1   *Legionella pneumophila* **macrophage infectivity potentiator protein appendage domains**

2   **modulate protein dynamics and inhibitor binding**

3

4   Wiedemann, C.[1, #], Whittaker[2, #], J.J., Pérez Carrillo[1, #], V.H., Goretzki[1, 3], B., Dajka[4,5], M., Tebbe[1], F.,

5   Harder[1], J.-M., Krajczy, P.[6], R., Joseph[3, 4, 5], B., Hausch[6,7], F., Guskov[2], A., Hellmich[1, 3, *], U.A.

6

7   [1]Faculty of Chemistry and Earth Sciences, Institute of Organic Chemistry and Macromolecular

8   Chemistry, Friedrich Schiller University Jena, Jena, Germany

9   [2]Groningen Institute for Biomolecular Sciences and Biotechnology, University of Groningen, 9747AG,

10   Groningen, The Netherlands

11   [3]Center for Biomolecular Magnetic Resonance, Goethe-University, Frankfurt/Main, Germany

12   [4]Institute for Biophysics, Goethe-University, Frankfurt/Main, Germany

13   [5]Department of Physics, Freie Universität Berlin, Germany

14   [6]Department of Chemistry and Biochemistry Clemens-Schöpf-Institute, Technical University

15   Darmstadt, Darmstadt, Germany

16   [7]Centre for Synthetic Biology, Technical University of Darmstadt, 64283 Darmstadt, Germany.

17

18

19   *Correspondence to UAH: ute.hellmich@uni-jena.de

20   #These authors contributed equally: C.W., J.J.W., V.H.P.C.

21

22   ORCIDs

23   CW: 0000-0003-4351-8857

24   JJW: 0000-0001-8966-111X

25   VHPC: 0000-0003-3580-4941

26   BG: 0000-0002-7721-6657

27   BJ: 0000-0003-4968-889X

28   AG: 0000-0003-2340-2216

29   UAH: 0000-0001-7162-285X

30

31

32

Abstract

Macrophage infectivity potentiator (MIP) proteins are widespread in human pathogens including *Legionella pneumophila*, the causative agent of Legionnaires' disease and protozoans such as *Trypanosoma cruzi*. All MIP proteins contain a FKBP (FK506 binding protein)-like prolyl-*cis/trans*-isomerase domain that hence presents an attractive drug target. Some MIPs such as the *Legionella* protein (*Lp*MIP) have additional appendage domains of mostly unknown function. In full-length, homodimeric *Lp*MIP, the N-terminal dimerization domain is linked to the FKBP-like domain via a long, free-standing stalk helix. Combining X-ray crystallography, NMR and EPR spectroscopy and SAXS, we elucidated the importance of the stalk helix for protein dynamics and inhibitor binding to the FKBP-like domain and bidirectional crosstalk between the different protein regions. The first comparison of a microbial MIP and a human FKBP in complex with the same synthetic inhibitor was made possible by high-resolution structures of *Lp*MIP with a [4.3.1]-aza-bicyclic sulfonamide and provides a basis for designing pathogen-selective inhibitors. Through stereospecific methylation, the affinity of inhibitors to to *L. pneumophila* and *T. cruzi* MIP was greatly improved. The resulting X-ray inhibitor-complex structures of *Lp*MIP and TcMIP at 1.49 and 1.34 Å, respectively, provide a starting point for developing potent inhibitors against MIPs from multiple pathogenic microorganisms.

Key Words: virulence factor; protein inhibitor complex; protein dynamics

Introduction

Bacterial parasitism is a wide-spread phenomenon and a serious health concern [1]. Approximately half of all identified Legionella species are associated with human disease, but most human legionellosis are caused by *Legionella pneumophila* [2]. In their natural fresh water reservoir habitat, these facultative intracellular gram-negative bacteria infect protozoa, where, protected from harsh environmental conditions, they find optimal conditions for intracellular replication while benefiting from the nutrient supply provided by the host [3]. After aspiration of contaminated water from e.g. air conditioners or hot water cisterns, *L. pneumophila* can also invade alveolar macrophages in the human lung thereby mimicking the infection of its native amoebal host [2,4,5]. This may result in severe infections such as Legionnaires' disease or the more benign Pontiac disease [2,4]. Although *Legionella* infections can be treated with antibiotics, Legionnaires' disease nonetheless has a mortality rate of ~10%, which is likely even higher in older or immunocompromised patients [6].

To promote uptake into a host cell, *L. pneumophila* relies on a number of proteins, including MIP (Macrophage infectivity potentiator), the first identified *L. pneumophila* virulence factor [7–9]. *Legionella pneumophila* MIP (*Lp*MIP) improves the environmental fitness of the bacterium and facilitates the progression of the early stages of the intracellular infection cycle [9–11]. Genetic deletion of *Lp*MIP results in a reduced intracellular replication rate [9,12].

*Lp*MIP is a homodimeric protein consisting of an N-terminal dimerization domain, a 65Å long, free-standing α-helix, the "stalk helix", and a C-terminal peptidyl prolyl-*cis/trans*-isomerase (PPIase) domain [13–15]. Structurally, the PPIase domain belongs to the FK506-binding proteins (FKBPs) named after their interaction with the natural product macrolide lactone FK506 [16,17]. In FKBPs, an amphipathic five-stranded β-sheet wraps around an α-helix thus forming a hydrophobic cavity that binds substrates and inhibitors [18]. Although the molecular mechanism of *Lp*MIP action in infection and its molecular target(s) remain unclear, it was implicated in host collagen interaction and subsequent epithelial barrier transmigration [19,20]. Nonetheless, the interaction between *Lp*MIP and collagen could not be mapped in detail, and instead of using classic chemical shift perturbations (CSP), NMR (nuclear magnetic resonance) spectroscopic PREs (paramagnetic relaxation enhancement) of spin-labeled collagen peptides had to be used to detect binding to *Lp*MIP [19], suggesting weak binding affinities. In contrast, unambiguous binding site mapping to *Lp*MIP has been shown by NMR CSP for rapamycin, a macrolide which also inhibits human FKBPs [21].

MIP proteins are widely expressed in many other human pathogenic microorganisms such as *Chlamydia spp.* [22], *Neisseria gonorrhoeae* [23], the entero-pathogen *Salmonella typhimurium* [24], *Pseudomonas aeruginosa* [25], and intracellular parasitic protozoans such as *Trypanosoma cruzi*, the causative agent of Chagas disease in South and Central America [26–28]. Hence, the PPIase domains of MIP proteins are attractive antimicrobial and antiparasitic drug targets [29], however their shallow ligand binding pocket and similarity to human FKBPs render selective drug design challenging [30,31]. No structures of a *Legionella* MIP with a synthetic inhibitor are available to date and, in the absence of a high-

3

91   resolution structure of a microbial MIP and human FKBP MIP in complex with the same synthetic

92   inhibitor, no side-by-side structural comparison is currently possible.

93   Limited structural information of *Lp*MIP is available, with only a crystal structure of the *apo* full-length

94   homodimer (PDB: 1FD9) [14] and the NMR solution structures of an *apo* and rapamycin-bound

95   truncation mutant (PDB: 2UZ5, 2VCD) [21]. This construct, *Lp*MIP$^{77-213}$, comprises the C-terminal half

96   of the stalk helix followed by the FKBP-like domain and thus resembles the architecture of the

97   constitutively monomeric *T. cruzi* MIP protein [26]. Other pathogens such as *Burkholderia*

98   *pseudomallei,* the bacterium causing melioidosis, express even more minimalistic MIP proteins, lacking

99   both dimerization domain and the complete stalk helix [32,33].

100   The role of MIP appendage domains, or the consequences of their (partial) absence, remains unclear.

101   However, homodimeric, full-length MIP from *Legionella pneuomophila* presents a unique opportunity

102   to explore the role of these domains in conformational flexibility and inhibitor binding. Here, we

103   combined X-ray crystallography, small angle X-ray scattering (SAXS), nuclear magnetic resonance

104   (NMR) and electron paramagnetic resonance (EPR) spectroscopy to uncover the importance of the

105   *Lp*MIP stalk helix for the protein's functional dynamics and to identify similarities and differences in

106   inhibitor binding among MIP proteins from various human pathogenic microorganisms and human

107   FKBPs.

108

109   **Results**

110   **Structural dynamics of full-length LpMIP and consequences of inhibitor binding**

111   Comparing our crystal structure of homodimeric full-length *Lp*MIP with improved resolution (1.71 Å,

112   PDB: 8BJC) to the previously published one (2.41 Å, PDB: 1FD9 [14]), revealed a ~18° splay between

113   the stalk helices in the two structures (Fig. 1A, B). The higher resolution of our electron density map

114   allowed unambiguous placement and assignment of all stalk helix residues (Fig. 1C, Table S1).

115   Furthermore, the stalk helix is not involved in crystal contacts suggesting that intrinsic conformational

116   heterogeneity is responsible for the observed differences between the two structures.

117   The splaying of the stalk helix, which emanates from the mid-helix residues ^{76}EFNKK^{80}, results in a

118   relative reorientation of the attached FKBP-like domains in the two crystal structures. Nonetheless, both

119   globular domains align with an RMSD of 0.214 Å (Fig. 1D). The main structural differences between

120   the two FKBP-like domain structures were observed in the loop between β-strand 4 and 5, resulting in

121   a different side-chain orientation for residue S189. Minor side-chain rearrangements were also seen for

122   residues D142, V158 and Y185 in the active site which may however result from the different

123   resolutions of the two structures.

124

125   Although microbial MIP proteins are promising drug targets, the structural similarity to human FKBP

126   proteins raises concerns about possible cross-reactivity and off-target effects [34,35]. Naturally

127   occurring inhibitors such as rapamycin (sirolimus) are large and chemically complex, poorly soluble in

4

128   water, and have severe immunosuppressive effects limiting their use to treat microbial infection [36].

129   The comparison of human FKBP and pathogenic microbial MIP proteins bound to a chemically simpler,

130   synthetic inhibitor molecules could thus present an important step towards improving ligand selectivity.

131   Recently, an inhibitory effect of [4.3.1] bicylic sulfonamides on *L. pneumophila* proliferation in

132   macrophages was demonstrated [34]. One such molecule, (1S,5S,6R)-10-((3,5-

133   dichlorophenyl)sulfonyl)-5-(hydroxymethyl)-3-(pyridin-2-ylmethyl)-3,10-diazabicyclo [4.3.1]decan-2-

134   one (JK095, Scheme 1), was co-crystallized with a human FKBP51 domain construct [34]. We thus

135   deemed this compound a promising candidate for structural studies with MIP proteins from human

136   pathogens and downstream structural comparison with human FKBPs. Isothermal titration calorimetry

137   (ITC) confirmed that JK095 indeed interacts with microbial MIP proteins and *Lp*MIP variants (see

138   below) and binds to full-length *Lp*MIP with a dissociation constant of 2.79 ± 0.4 µM (Fig. S1).

139   We also determined the structure of full-length *Lp*MIP in complex with JK095 by X-ray crystallography

140   at 2.4 Å resolution (PDB: 8BJD) (Fig. 2A). The most notable structural differences between the crystal

141   structures of *apo* and JK095-bound *Lp*MIP is the rearrangement of the loop connecting β-strands β4 and

142   β5 near the stalk helix. Ligand binding to *Lp*MIP in solution was probed by titrating ^{2}H, ^{15}N-labeled

143   *Lp*MIP with JK095 (Fig. 2B, C). Chemical shift perturbations were observed in the FKBP-like domain,

144   consistent with the binding site identified in the crystal structure. In addition, residues within the FKBP

145   domain facing the stalk helix, the stalk helix and the dimerization domain show chemical shift

146   perturbations upon JK095 binding. In the *apo* state, the amide resonances between residues ~57-76 in

147   the N-terminal half of the *Lp*MIP stalk helix show severe line broadening and were thus not visible in

148   the protein's ^{1}H, ^{15}N-HSQC NMR spectrum (Fig. 2C, Fig. S2A). Upon addition of JK095, these

149   resonances become visible in the spectra. This suggests that motions in the µs-ms timescale, which are

150   responsible for the peak broadening in the NMR spectrum, are quenched by the ligand whose interaction

151   with the FKBP-like domain is allosterically communicated into the stalk helix and dimerization domain.

152   While crystallographic B-factors are generally less well suited to assess dynamic changes, the observed

153   lower values in the presence of JK095 agree with the NMR spectroscopic results (Fig. 2D, E).

154

155   To assess the structural dynamics of *Lp*MIP both locally and on a global scale in solution, we combined

156   NMR relaxation studies with pulsed electron paramagnetic resonance (EPR) spectroscopy and small

157   angle X-ray scattering (SAXS) (Fig. 3, Fig. S3-S6). NMR relaxation experiments informing on fast, ps-

158   ns amide bond fluctuations and dynamics overlying the protein's global rotational dynamics show that

159   *Lp*MIP is relatively rigid on the assessed timescale, except for the very N-terminus, the linker between

160   β3a and β3b, the linker between β4 and β5 and the C-terminus (Fig. S3). In contrast to the influence of

161   JK095 on the protein dynamics on slower timescales, as was apparent through the changes in line

162   broadening, fast backbone dynamics were not, or only marginally affected by the inhibitor.

163

164   The results from EPR spectroscopy and SAXS further provide evidence of the high flexibility of *Lp*MIP

165   in solution (Fig. 3). *Lp*MIP does not contain native cysteine residues. Thus, single cysteine mutants in

166   the middle of the stalk helix (*Lp*MIP K80C) and at the C-terminal end of the FKBP-like domain (*Lp*MIP

167   S208C) were introduced and labeled with nitroxide spin labels (Fig. 3A, Fig. S4, S5). Continuous wave

168   EPR confirmed a satisfactory labeling efficiency at both positions (Fig. 3B).

169   Pulsed EPR spectroscopy (pulsed electron-electron double resonance (PELDOR, also known as DEER))

170   was used to determine the distances between the two spin-labeled sites, and the measurements were

171   compared to simulations of the spin pair distance distributions based on the available crystal structures

172   (Fig. 3C-E, Table S2). The distance distributions obtained from spin labeled *Lp*MIP K80C and S208C

173   were broader than expected from the crystal structures, indicating that these structures represent only a

174   subset of conformers in solution. Upon addition of JK095, no significant changes were observed for

175   *Lp*MIP K80C, while for S208C the overall distribution shifted towards shorter distances. This could be

176   explained e.g. by structural changes of the two FKBP domains moving closer together. Of note, the

177   related NMR data show that at a molar protein:inhibitor ratio of 1:3 (n/n), the complex is already fully

178   saturated. The EPR measurements were carried out with a protein:inhibitor ratio of 1:5, indicating that

179   even when fully occupied, the "closed" conformation is only transiently populated.

180   Extensive structural dynamics of *Lp*MIP in solution are also apparent from SEC-SAXS experiments

181   (Fig. 3F-I, Fig. S6, Table S3). Here, the *Lp*MIP scattering profiles did not match a simulated scattering

182   curve using the available crystal structure, again suggesting a more complex conformational ensemble

183   in solution. For a better fit with the experimental SAXS data of *Lp*MIP in solution, SREFLEX modeling

184   was carried out [37] and *Lp*MIP structural models with straight and kinked stalk helices were obtained

185   (Fig. 3H, I). While there were no discernible differences between the *apo* and JK095-bound state in the

186   *Lp*MIP SREFLEX models, which may reflect the loss of JK095 during the size exclusion run (see

187   below), the SAXS data show high domain flexibility concurrent with the EPR experiments.

188

189   **The appendage domains influence LpMIP dynamics and stability**

190   Due to their high expression yields and solubility, deletion rather than full-length constructs have

191   frequently been used for structural studies of both MIP and FKBP inhibitor complexes [21,38].

192   However, this may not only inadequately reflect the complexity of the therapeutic target, but also

193   compounds a lack of understanding how the appendage domains affect protein structural dynamics and

194   inhibitor binding. This question is exacerbated by our observation that ligand binding to the FKBP-like

195   domains is sensed throughout the entire protein (Fig. 2).

196   In combination with our structural and spectroscopic studies on full-length *Lp*MIP, the modular

197   architecture of *Lp*MIP provides a unique opportunity to explore such questions through deletion

198   mutants. To emulate the structural diversity of MIP proteins from other human-pathogenic microbes,

199   we generated two shortened *Lp*MIP constructs, *Lp*MIP$^{77-213}$ and *Lp*MIP$^{100-213}$ (Fig. S7A). *Lp*MIP$^{77-213}$,

200   containing the FKBP-like domain and a bisected stalk helix thus resembling *T. cruzi* MIP [26], is the

6

201 construct typically used in *in vitro* ligand binding studies [20,21,39]. LpMIP[100-213], which consists solely

202 of the FKBP domain, resembles e.g. *B. pseudomallei* MIP [33]. Both LpMIP[77-213] and LpMIP[100-213] are

203 monomeric and structurally intact as seen by size exclusion chromatography (SEC) and circular

204 dichroism (CD) spectroscopy (Fig. S7B-D). In a fluorescence-based assay, we saw that the melting

205 temperature (T_m) depended greatly on the protein's appendage domains. (Fig. 4A). With 51.4 ± 0.3 °C,

206 the T_m of LpMIP[100-213] was found to be ~14°C below that of the slightly longer construct LpMIP[77-213]

207 (64.6 ± 0.6 °C) and ~9 °C lower than that of full-length LpMIP (60.7 ± 0.3 °C) (Fig 4A top). In all three

208 constructs, addition of JK095 led to an increase in the melting temperature commensurate with protein

209 stabilization upon inhibitor binding (Fig. 4A bottom). However, this effect was less pronounced for

210 LpMIP[100-213] ($\Delta T_{m(JK095\text{-}apo)} = +2.8$ °C) compared to both longer constructs ($\Delta T_{m(JK095\text{-}apo)} = +3.8$ °C). This

211 may reflect the strongly reduced binding affinity of JK095 to LpMIP[100-213] ($K_d = 45.8 \pm 20$ µM) compared

212 to LpMIP[77-213] ($K_d = 2.5 \pm 0.5$ µM) and full-length LpMIP ($K_d = 2.8 \pm 0.4$ µM) (Fig. S1). The differences

213 in T_m and inhibitor binding affinity suggest that the appendage domains, in particular the part of the

214 stalk helix directly preceding the FKBP domain, play an important role in protein stability and ligand

215 binding.

216

217 To investigate the structural crosstalk between appendage and FKBP domains in LpMIP in more detail,

218 we used NMR spectroscopy. With the backbone assignments of all three LpMIP constructs in the *apo*

219 and JK095-bound states (Fig. S2), the chemical shifts for residues within the FKBP-like domains were

220 compared (Fig. 4C, D). In the absence of inhibitor, there were only minor differences between full-

221 length LpMIP and LpMIP[77-213], except for the very N-terminal residues where the cleavage site is located

222 (Fig 4C top, orange). Interestingly, differences between the two constructs became slightly more

223 pronounced in the presence of JK095, particularly for residues in the β4/β5 loop (Fig 4C bottom,

224 orange).

225 In contrast, the comparison between full-length LpMIP with LpMIP[100-213] already showed strong

226 chemical shift perturbations in the *apo* state (Fig 4C top, cyan). Most notable were the effects in the

227 vicinity of residue 160 within the canonical ligand binding site, and between residues 180 and 200,

228 which are part of the long loop between β-strands 4 and 5 and form an interaction network with the C-

229 terminal half of the stalk helix (Fig. 4D, E). Furthermore, in the ^{1}H, ^{15}N-HSQC spectrum of LpMIP[100-

230 213], no or extremely weak resonances for S115-N117, K146/T147, I159 and R188 were observed, while

231 these were clearly visible in both longer constructs (Fig. 4D, E, Fig. S2). This suggests that these regions

232 show altered dynamics in the absence of the stalk helix. However, except for residue I159 as well as

233 R188 in the β4/5 loop, none of these residues are directly involved in FKBP/stalk helix interactions or

234 part of the canonical ligand binding site, thus suggesting allosteric effects on the canonical binding site

235 through the stalk helix. Potentially, such long-range crosstalk could be mediated through a hydrophobic

236 interaction network between the stalk helix and FKBP-like domain (Fig. 4E).

237   Since the residues across all three full-length *Lp*MIP domains showed no significant differences in their

238   respective backbone dynamics in the ps-ns timescale in {^{1}H}^{15}N-hetNOE experiments between the *apo*

239   and the JK095-bound states (Fig. S3A), stalk helix removal seems to mostly affect slower, µs-ms

240   motions within the FKBP-like domain. In the absence of the stalk helix, increased hetNOE values for

241   *Lp*MIP$^{77-213}$ and *Lp*MIP$^{100-213}$ indicate slightly subdued backbone dynamics of the FKBP-like domain

242   within the loops connecting β3a/β3b and β4/β5, both in the absence and presence of JK095 (Fig. S3B,

243   C).

244

245   **Role of the appendage domains for FKBP-like domain inhibitor binding**

246   To gauge a possible structural role of the appendage domains for ligand binding in *Lp*MIP as suggested

247   by our thermostability assays and NMR data (Fig. 4), we determined the crystal structures of *Lp*MIP^{77-}

248   ^{213} (PDB: 8BK5) and *Lp*MIP$^{100-213}$ (PDB: 8BK6) with JK095 at 2.26 and 1.49 Å resolution, respectively

249   (Fig. 5A). These complement the crystal structure of full-length *Lp*MIP with JK095 (PDB: 8BJD, Fig.

250   2). The largest structural differences across all three *Lp*MIP constructs are observed in the β4/β5 loop,

251   while the side chains of the active site residues adopted nearly identical orientations. JK095 bound to

252   *Lp*MIP$^{77-213}$ adopted a very similar binding stance as seen in the canonical binding pocket of full-length

253   *Lp*MIP (Fig. 5A, B). However, in *Lp*MIP$^{77-213}$, the inhibitor's hydroxymethyl group adopted two

254   orientations while in full-length *Lp*MIP, only the orientation facing away from the sidechain of D142

255   was observed, thereby forgoing the formation of a possible hydrogen bond interaction. Furthermore, the

256   pyridine ring nitrogen was 2.7 Å away from the Y185 sidechain hydroxyl group in *Lp*MIP$^{77-213}$, while

257   this distance increased to 3.7 Å in full-length *Lp*MIP.

258   In contrast to the two longer constructs, the inhibitor binding site in *Lp*MIP$^{100-213}$ was not clearly defined

259   in the crystal structure (Fig. S8). To verify the possibility of drastically altered ligand interaction to the

260   FKBP-like domain in the absence of the appendage domains in solution, we compared the chemical shift

261   perturbations of the three ^{15}N-labeled *Lp*MIP constructs titrated with JK095 (Fig. 5D, E, Fig. S2A-C).

262   As expected, the chemical shift changes in full-length *Lp*MIP and *Lp*MIP$^{77-213}$ agree with the binding

263   site observed in the respective complex crystal structures. In stark contrast, addition of JK095 to

264   *Lp*MIP$^{100-213}$ affected a significantly larger number of residues and the chemical shift perturbation pattern

265   was not restricted to the canonical ligand binding site. Of note, *Lp*MIP$^{100-213}$ crystallized as a parallel

266   dimer with the loop between β4 and β5 mediating many of the dimer contacts (PDB: 8BK6, Fig S8).

267   These loops showed the largest structural differences between the two *Lp*MIP$^{100-213}$ protomers in the unit

268   cell and the largest chemical shift changes upon addition of JK095 in the NMR experiments. We thus

269   wondered whether transient oligomerization could be responsible for the extensive JK095-dependent

270   chemical shift perturbations in the 12 kDa *Lp*MIP$^{100-213}$ construct. Under the assumption of isotropic

271   tumbling, a rotation correlation time τ_c of 5.6 ns can be approximated according to the Stokes-Einstein

272   equation for a spherical globular, monomeric protein of that size at 25 °C (see material and methods for

273   details). By applying an empirical formula [40], a τ_c value of 7.3 ns can be derived for a 12 kDa

8

274   molecule. Accordingly, neither the overall narrow line widths in the NMR spectra of ^{15}N-labeled

275   LpMIP$^{100-213}$ (Fig. S2C), nor the experimentally determined rotation correlation times ($\tau_c = 6.8 \pm 0.9$ ns

276   for the *apo* protein, $\tau_c = 6.4 \pm 0.7$ ns in the presence of JK095) are indicative of inhibitor-induced dimer

277   formation of LpMIP$^{100-213}$. Rather, the extensive NMR chemical shift perturbations in LpMIP$^{100-213}$ upon

278   addition of JK095 are likely caused by the non-specific interaction with the inhibitor. This finding

279   supports the notion that the LpMIP appendage domains, particularly the C-terminal half of the stalk

280   helix, play a decisive role in ligand binding to and dynamics within the FKBP domain.

281

282   **Comparison of LpMIP and human FKBP51 in complex with the same [4.3.1]-aza-bicyclic**

283   **sulfonamide inhibitor**

284   LpMIP$^{77-213}$ shares 32 % sequence similarity with a construct of human FKBP51 (residues 16-140) that

285   was recently co-crystallized with JK095 [41]. The two complex crystal structures (PDB IDs: 50BK,

286   8BK5) align with a backbone RMSD of 0.776Å (Fig. 6A). All residues interacting with JK095 are

287   conserved between the two proteins (Fig. 6B). A conserved tyrosine residue (Y113/Y185 in

288   FKBP51/LpMIP) responsible for forming a H-bond to the nitrogen of the pyridine or bicycle of the

289   inhibitor adopted the same orientation in both proteins. The sidechain of residue 159 forms a

290   hydrophobic lid below the bi-cycle by forming van der Waals contacts with the inhibitor's bicycle

291   carboxy group. In addition, a barrage of aromatic residues in either protein nestles the bi-cyclic inhibitor

292   core from below (Fig. 6B).

293   The inhibitor's pyridine group, bi-cyclic core and sulfonamide group align well between the two

294   proteins, only the di-chlorophenyl moiety is slightly differently tilted. Slight structural variations in the

295   β3a-strand within the FKBP domain were found between FKBP51 and LpMIP, namely across residues

296   ^{67}FDS^{69} and ^{141}FDS^{143}, respectively. The aromatic residue in this stretch may stabilize the di-

297   chlorophenyl moiety through T-shaped π stacking. Inhibitor binding may also be affected by the

298   structural and sequential differences in the loop connecting β4 and β5 (^{117}GSLPKI^{122} in FKBP51 and

299   ^{189}SVGGPI^{194} in LpMIP). Sitting on top of the di-chlorophenyl moiety of the ligand, the respective

300   isoleucine residue within this stretch, together with the abovementioned phenylalanine in β3a, form a

301   hydrophobic platform against which the di-chlorophenyl ring rests. In the case of FKBP51, the sidechain

302   of S118 may additionally contact one chloro-substituent and thereby help to orient it. In contrast, the

303   loop orientation observed in the LpMIP$^{77-213}$ crystal structure may disfavor interactions of either of the

304   two chlorine groups with loop sidechains. The structural perturbation of the $^{67/141}$FDS$^{69/143}$ motif in the

305   β3a-strand also led to slightly different orientations of its central aspartic acid sidechain when comparing

306   the structures of FKBP51$^{16-140}$ and LpMIP$^{77-213}$. In both cases, the bound JK095 ligand's hydroxymethyl

307   group adopts two orientations. However, in FKBP51$^{16-140}$, neither orientation comes close enough to

308   form a hydrogen bond with the aspartic acid side chain of D68 (O-O distance 4.0 Å). In contrast, in

309   LpMIP$^{77-213}$, in one of the two orientations the distance to the corresponding residue D142 is reduced by

310   0.9 Å compared to FKBP51[16-140]. In the other orientation, the inhibitor hydroxyl group can form

311   hydrogen bonds with water molecules (see below).

312

Methylation leads to improved inhibitor binding to MIPs from different pathogenic microorganisms

315   It was recently observed that the stereospecific introduction of a methyl group at the C_α position of the

316   pyridine substituent of bicyclic [4.3.1]-aza-amide inhibitors significantly increased their affinity for

317   FKBP51 due to displacement of a surface water molecule and the associated entropic gain [41]. JK095

318   does not carry such a methyl group and in our complex structure with LpMIP[77-213], we observed a

319   crystallographic water in a similar surface position as the one that originally inspired the inhibitor

320   methylation studies for human FKBP51 [41] (Fig. 7A). We thus wondered whether inhibitor methylation

321   may be used to improve the affinity of bicyclic sulfonamides for MIP proteins from pathogenic

322   microorganisms. To test this hypothesis, we introduced a methyl group into JK095, yielding JK236

323   (Scheme 1) and determined the co-crystal structure of LpMIP[77-213] with JK236 at 1.49 Å resolution

324   (PDB: 8BJE) (Fig. 7B-D).

325   Overall, the structures of LpMIP[77-213] with JK095 and JK236 align with an RMSD of 0.283 Å and show

326   no notable differences in protein sidechain or inhibitor conformations. Together with NMR chemical

327   shift perturbation data of ^{15}N-labeled LpMIP[77-213] titrated with JK095 or JK236 (Fig. 7E, F, Fig. S2D),

328   this confirmed that both ligands interact in a highly similar fashion with the LpMIP FKBP-like domain.

329   Furthermore, pulsed EPR measurements of spin-labeled full-length LpMIP K80C and LpMIP S208C

330   showed that JK236 affects the structural ensemble of full-length LpMIP in a similar manner as JK095

331   (Fig. 7G, Fig. S5, S6).

332   Nonetheless, the binding affinity of JK236 to LpMIP[77-213] and full-length LpMIP was increased by

333   roughly one order of magnitude for the methylated ($K_d = 440 \pm 204$ nM and 391 ± 48 nM), compared to

334   the unmethylated compound (2.5 ± 0.5 µM and 2.8 ± 0.4 µM) (Fig. S1). In line with a less defined

335   inhibitor interaction site in LpMIP[100-213], this increase in affinity was much less pronounced for the

336   shortest LpMIP construct ($K_d = 45.8 \pm 20.4$ µM vs 5.1 ± 1.4 µM for JK095 and JK236, respectively). A

337   surface water molecule is indeed displaced in the JK236 co-crystal structure compared to the complex

338   with JK095 (Fig. 7A). While the two inhibitors bound to LpMIP superimpose nearly perfectly, the

339   orientation of the hydroxymethyl group is fixed in JK236 in contrast to the two orientations observed

340   for JK095. In JK236, the hydroxymethyl group faces away from the sidechain of D142 and instead

341   exclusively forms a hydrogen bridge with a water molecule. At a resolution of 1.49 Å, the additional

342   methyl group in JK236 can also be placed unambiguously in the crystal structure and is seen to point

343   into the solvent where it does not undergo any protein contacts but rather displaces a water molecule

344   (Fig. 7A). This shows that the methylation of bicyclic ligands to obtain high-affinity binders through

345   surface water displacement is feasible for LpMIP and may constitute a general concept for FKBPs as

346   well as microbial MIPs.

347

348   To gauge whether methylation for improved binding is indeed applicable to MIPs from other human

349   pathogens including those of eukaryotic origin, we turned to the protozoan *Trypanosoma cruzi*, the

350   causative agent of Chagas disease. With a free-standing stalk helix and a prototypical FKBP domain,

351   the *T. cruzi* MIP protein (*Tc*MIP) structurally resembles the *Lp*MIP[77-213] construct lacking the

352   dimerization domain and N-terminal half of the stalk helix (Fig. 8).

353   Similar to *Lp*MIP, ligand binding to *Tc*MIP was significantly improved for the methylated compound

354   (K_d = 150 ± 68 nM (JK236) versus 594 ± 55 nM (JK095) (Fig. S1). Our crystal structure of *Tc*MIP in

355   complex with JK236 (PDB: 8BK4) at 1.34 Å resolution confirms the interaction of JK236 with the

356   canonical binding site in the FKBP-like domain and a highly similar interaction mode as seen for *Lp*MIP

357   (Fig. 8, Fig. S9).

358   The complex structure aligns to the previously published structure of *apo Tc*MIP (PDB: 1JVW) [26]

359   with an RMSD of 0.499 Å (Fig. 8A). The largest differences between the two proteins are seen again in

360   the loop connecting β-strands 4 and 5, as well as in β-strand 3a. In the *Tc*MIP *apo* structure, multiple

361   water molecules are found around the substrate binding site which are absent with JK236, but no surface

362   water molecule is seen in the same position as detected in JK095-bound FKBP51 [34] and *Lp*MIP.

363   However, due to the lack of a complex structure of *Tc*MIP with JK095, it is difficult to assess the

364   consequences of inhibitor methylation on water occupancy in *Tc*MIP in detail. Nonetheless, the similar

365   gain in binding affinity through the introduction of the methyl group into the bi-cyclic inhibitor indicates

366   a similar mode of action that can be exploited for the development of high-affinity binders against MIP

367   proteins from various pathogens. The availability of two structures of MIP proteins from highly diverse

368   pathogenic microorganisms in complex with the same synthetic inhibitor now also provides a unique

369   opportunity to elucidate the possibility to generate pan-inhibitors.

370

371   **Discussion**

372   The role of MIPs as widespread microbial virulence factors has spurred efforts to develop inhibitors

373   targeting the MIP FKBP-like domain as the most conserved MIP domain. However, many MIP proteins

374   contain additional appendage domains of unknown function. This prompted us to investigate the

375   interdomain crosstalk and dynamics of the homodimeric *Legionella pneumophila* MIP protein as a

376   representative model system for multi-domain MIPs in more detail.

377   Intrinsic structural flexibility seems to be a hallmark of homodimeric MIP proteins from pathogenic

378   microorganisms [42]. Not only did we notice significant stalk helix splaying between the two available

379   crystal structures of full-length *Lp*MIP in the absence of a ligand, but a recently published structure of

380   unliganded, homodimeric *P. aeruginosa* FkbA, which shares the same three-domain architecture,

381   showed both straight and bent stalk helices in the crystal structure [25]. It has been suggested that

382   variations in crystal structures are a good proxy for dynamics in solution [43] and in the case of *Lp*MIP,

383   we can support and extend this notion with EPR and NMR spectroscopy as well as SAXS. Our crystal

384 structures provide a glimpse of the protein's dynamics, but the full extent of its domain gymnastics in

385 solution required a multi-faceted approach.

386 Using NMR spectroscopy, we identified a dynamic hotspot in the central stalk helix of *Lp*MIP. This is

387 also the region that shows extensive kinking in our SAXS SREFLEX models. A difference in "bending"

388 of the central stalk helix was mentioned previously for a co-crystal of full-length *Lp*MIP with FK506

389 [14], although the corresponding data set has never been submitted to the PDB and thus cannot be

390 analyzed in detail here. We saw that binding of a bi-cyclic vinylsulfone inhibitor led to a rigidification

391 of the N-terminal half of the stalk helix. Likewise, Pervushin and colleagues reported that the *E. coli*

392 FkpA stalk helix rigidifies in the presence of a client protein and led to reduced interdomain mobility

393 [42].

394 Comparing JK095-bound *Lp*MIP[77-213] with the rapamycin-bound protein (Fig. S10), shows the relative

395 displacement of the ligand enclosing sidechains and indicates that the active site of *Lp*MIP displays a

396 conformational flexibility commensurate with its ability to bind to differently sized ligands. Across all

397 our structures, the β4/β5 loop, which interacts with the stalk helix and may thus serve as a substrate-

398 selective communication node between stalk and FKBP-like domain, showed the most structural

399 variations. In contrast to previous observations with rapamycin [21], no significant rigidification of

400 FKBP-like domain loops on very fast timescales was observed with JK095, while slower dynamics were

401 quenched throughout the protein upon ligand binding. Different inhibitor molecules could thus

402 potentially mimic the structural and dynamic consequences of diverse, yet unidentified, native ligands.

403 Unfortunately, the affinity of collagen peptides, the only known native *Lp*MIP substrate to date [19,20],

404 is too low for detailed structural and dynamic analysis.

405 Furthermore, the addition of bi-cyclic inhibitors led to a population shift but not a full transition to a

406 "closed" conformation with decreased distances between the FKBP-like domains in our EPR

407 experiments. Whether this is a general feature of *Lp*MIP ligands or unique to the tested inhibitors is

408 unknown. Future ligand screening could explore whether the ability of ligands to shift the *Lp*MIP

409 conformational ensemble to a closed state correlates with its antimicrobial efficiency.

410 We could also show that the *Lp*MIP domains engage in bidirectional crosstalk. Ligand binding at the

411 FKBP-like domain affected the stalk helix and dimerization domain, and, in turn, stalk helix deletion

412 reduced protein stability and, surprisingly, led to the loss of a defined ligand binding mode. The

413 allosteric modulation of ligand binding by the C-terminal half of the stalk helix has interesting

414 implications for ligand recognition and regulation of MIP proteins from other pathogenic species, such

415 as *Burkholderia pseudomallei*, which naturally lack a stalk helix and dimerization domain [33].

416 Deletion constructs of MIP proteins have been commonly used to study inhibitor binding. Our data

417 suggests that a construct retaining the C-terminal half of the stalk helix is suitable for most applications,

418 but there are nonetheless some differences to consider. The ligand orientation and flexibility in certain

419 inhibitor moieties differ slightly between full-length LpMIP and LpMIP$^{77-213}$. The increased melting
420 temperature of LpMIP$^{77-213}$ may indicate that the stabilization of the FKBP domain by the stalk helix' C-
421 terminal end is counteracted by the protein's flexibility in the N-terminal half. Complete deletion of the
422 stalk helix has negative consequences for both protein stability and ligand interactions.

423 Bi-cyclic sulfonamides have antiproliferative effects against *L. pneumophila* and *Chlamydia*
424 *pneumoniae*, which both express MIP proteins [34]. This suggests that the bicyclic sulfonamide scaffold
425 is a promising starting point for drug development. Our results on *T. cruzi* MIP suggest that both
426 prokaryotic and eukaryotic MIP proteins can be targeted with a high-affinity pan-inhibitor, and lessons
427 from human FKBPs such as site-specific methylation [41] can be exploited to improve inhibitor affinity
428 for microbial MIPs. However, the structural similarities between MIPs and FKBPs pose challenges,
429 particularly since FKBP inhibition leads to immunosuppression, the opposite of the desired effect in
430 fighting severe infections. Here, we could directly compare a microbial MIP with a human FKBP in
431 complex with the same synthetic ligand for the first time. In a previous NMR study on FKBP51, the
432 central aromatic residue in the β3a-strand, was seen to flip in and out of the binding pocket, a process
433 important for ligand selectivity [44]. The residues stabilizing the "outward" position (FKBP51 K58,
434 K60 and F129) are not fully conserved in LpMIP (T132, R134, F202). Hence ring flipping might be an
435 important distinguishing feature between the two proteins. Additional structures and dynamic studies of
436 human FKBPs and microbial MIPs in complex with the same ligands, possibly with other molecular
437 scaffold architectures, may be helpful in making further progress in this area.

438 In summary, we found that in *Legionella pneumophila* MIP, the stalk helix decisively modulates ligand-
439 binding behavior of the FKBP-like domain, the most conserved domain across all MIP proteins. This,
440 together with the high intrinsic flexibility of MIP proteins and the ability to engage with structurally
441 diverse ligands, suggests that MIP appendage domains can be used to fine-tune substrate responses and
442 suggest they play a contextual role in the survival and replication of pathogenic microorganisms.

443

444 **Material and Methods**

445 **Cloning, protein expression and purification**

446 Genes coding for *Legionella pneumophila* LpMIP$^{1-213}$, LpMIP$^{77-213}$, LpMIP$^{100-213}$ and *Trypanosoma cruzi*

447 TcMIP with a His$_6$-tag were obtained from GenScript (Piscataway Township, NJ, USA) and cloned into

448 a pET11a vector. Single cysteine mutants for EPR spectroscopy were introduced at positions K80C and

449 S208C in LpMIP$^{1-213}$ via site directed mutagenesis using the following primer pairs:

450 K80C forward: 5´-CCGCGGAGTTTAACAAGTGCGCGGATGAAAACAAGG-3´

451 K80C reverse 5´- ACCTTGTTTTCATCCGCGCACTTGTTAAACTCCGCG–3´

452 S208C forward 5´- TAAGATTCACCTGATCTGCGTGAAGAAAAGCAG – 3´

453 S208C reverse 5´- CTGCTTTTCTTCACGCAGATCAGGTGAATCTTA – 3

454 Freshly transformed *E coli.* BL21 gold (DE3) cells were grown at 37 ºC to an OD$_{600}$ of 0.6 and then

455 induced with 1 mM IPTG and grown overnight at 20 ºC. ^{2}H, ^{15}N-labeled LpMIP$^{1-213}$ was obtained by

456 growing cells in commercially available Silantes OD2 *E. coli* medium (Silantes GmbH, Munich,

457 Germany). ^{13}C, ^{15}N-labeled LpMIP$^{77-213}$ and LpMIP$^{100-213}$ were obtained by growing cells in minimal

458 medium with ^{15}N-NH$_4$Cl and ^{13}C-glucose as the sole nitrogen and carbon sources. Cells were harvested

459 by centrifugation (5000×g, 10 min, 4 °C). The cell pellet was frozen in liquid nitrogen and stored at

460 – 20 °C until further use.

461 For purification of LpMIP$^{1-213}$ and LpMIP$^{77-213}$, the cell pellet was dissolved in lysis buffer (20 mM Tris

462 pH 8, 20mM Imidazole pH 8, 300 mM NaCl, 0.1 % Tx100, 1 mM DTT, 1 mM benzamidine, 1 mM

463 PMSF, DNAse, RNAse and lysozyme). Cells were disrupted passing them three times through a

464 microfludizer (Maximator) at 18,000 psi. Membranes and cell debris were pelleted at 48,380xg, 30 min,

465 4 °C and the supernatant was loaded onto a NiNTA column (Qiagen, Hilden, Germany) previously

466 equilibrated with washing buffer (20 mM Tris pH 8, 300 mM NaCl and 20 mM imidazole). After

467 washing with 10 CV (column volumes) of washing buffer, the protein of interest was eluted with 5 CV

468 of elution buffer (20 mM Tris pH 8, 300 mM NaCl and 500 mM imidazole pH 8). Proteins were dialyzed

469 overnight at 4 ºC in 20 mM Tris pH 8, 300 mM NaCl in the presence of His-tagged TEV protease (1:20

470 mol/mol) to cleave the His-tag from the MIP constructs.

471 Dialyzed protein was then loaded onto a fresh NiNTA column. The flow through was collected and the

472 column was washed with 4 CV of washing buffer to obtain the maximum amount of tag-free MIP

473 protein. For the purification of LpMIP$^{100-213}$ the same protocol was applied, with all buffers adjusted to

474 pH 7. After concentration, the proteins were loaded on a size exclusion column (HiLoad 16/600

475 Superdex 200 pg, Cytiva, Freiburg, Germany) equilibrated with size exclusion buffer (20 mM Tris pH 7,

476 150 mM NaCl for LpMIP$^{77-213}$ and LpMIP$^{100-213}$ and 50 mM Tris pH 7, 150 mM NaCl for LpMIP$^{1-213}$).

477 The fractions containing pure protein were pooled and sample purity was verified by SDS-PAGE.

478

479 **Crystallization, data collection and structure determination of LpMIP inhibitor complexes**

14

480   Following size exclusion chromatography, each of the proteins were kept in a solution of 20 mM Tris

481   and 150 mM NaCl at pH 7.0 and were concentrated to 10 mg/mL using a 10,000 MWCO concentrator.

482   Each protein was mixed with the crystallization buffer in a ratio of 2:1, and, where appropriate, with a

483   1:5 molar ratio of inhibitor. Inhibitors were synthesized as previously described [34,41]. All crystals

484   were obtained using sitting drop vapor diffusion via custom screens with the following conditions:

485   LpMIP$^{1-213}$ 20 %(w/v) PEG 6000, 500 mM zinc acetate dihydrate, 100 mM MES, pH 6.0. LpMIP^{1-}

486   ^{213}JK095 15 %(w/v) PEG 6000, 500 mM zinc acetate dihydrate, 100 mM MES, pH 6.5. LpMIP$^{100-213}$

487   JK095 20 %(w/v) PEG 8000, 500 mM zinc acetate dihydrate, 100 mM MES, pH 5.8. LpMIP$^{77-213}$ JK095

488   20 %(v/v) 2-propanol, 0.2 M sodium citrate tribasic dihydrate, 0.1 M HEPES, pH 7.5. LpMIP$^{77-213}$ JK236

489   18 %(w/v) PEG 8000, 0.2 M zinc acetate, 0.1 M sodium cacodylate, pH 6.5. TcMIP JK236 30 %(v/v)

490   MPD, 0.2 M ammonium acetate, 0.1 M sodium citrate, pH 5.6. Crystals were briefly soaked in 30 %(v/v)

491   glycerol for cryo-protection and subsequently flash-frozen in liquid nitrogen in preparation for

492   diffraction experiments at synchrotron energy. Data were collected at beam line ID23-1 and ID30A-3

493   (ESRF, Grenoble).

494   Crystals of the MIP series diffracted between 1.3 and 2.4 Å resolution (Table 1). Data were processed

495   with XDS [45] and structures were solved by Molecular Replacement with Phaser [46] using previously

496   published models of MIPs (PDB ID: 1FD9, 1JVW). Manual rebuilding was performed with COOT [47]

497   and refinement with Refmac [48]. The refined models were deposited into the PDB repository with the

498   following IDs: 8BJC, 8BJD, 8BJE, 8BK4, 8BK5, 8BK6. Images were prepared using Pymol

499   (Schrödinger, LLC), CorelDRAW (Corel), UCSF ChimeraX [49] and Blender (Blender Foundation).

500

501   **Analytical Size-exclusion chromatography (SEC)**

502   20 µM of purified LpMIP constructs (LpMIP$^{1-213}$, LpMIP$^{77-213}$ or LpMIP$^{100-213}$) in 20mM Tris pH 7, 150

503   mM NaCl were used. For the *apo* state protein, a final concentration 0.02% DMSO was added. A 5-fold

504   molar excess of JK095 in DMSO was added (0.02% final DMSO concentration). Samples were injected

505   on a Superdex 200 Increase 10/300 GL (Cytiva) column via an NGC chromatography system (BioRad).

506

507   **Circular Dichroism (CD) spectroscopy**

508   CD measurements were conducted on a Jasco J-1500 CD spectrometer (Jasco, Gross-Umstadt,

509   Germany) with 1 mm quartz cuvettes using 3.5 µM protein in 5 mM Tris pH 7 and 2.5 mM NaCl.

510   Spectra were recorded at 25 ℃ in a spectral range between 190 – 260 nm with 1 nm scanning intervals,

511   1.00 nm bandwidth and 50 nm/min scanning speed. All spectra were obtained from the automatic

512   averaging of five measurements.

513

514   **Isothermal Titration Calorimetry (ITC)**

515   Experiments were performed in an isothermal titration calorimeter (Microcal ITC200 - Malvern

516   Panalytical) at 25 ℃ with a reference power of 11 µCal/sec, an initial delay of 120 seconds and a stirring

517   speed of 750 rpm. Protein concentration within the cell was between 20 and 40 μM and ligand
518   concentration in the syringe was between 0.5 and 1 mM. Protein and inhibitors (JK095 and JK236) were
519   prepared in 20 mM Trips pH 8, NaCl 150 mM and 5% DMSO. For each titration, 20 injections (spacing
520   between injections was 180 sec, duration was 0.4 sec) of 2 μL inhibitor solution were carried out. The
521   curves were fitted using Origin.

522

523   **NMR spectroscopy**

524   All NMR spectra were obtained at 298. K on 600 MHz Bruker AvanceIII HD or Neo NMR spectrometer
525   systems equipped with 5-mm triple resonance cryo-probes. The spectrometers were locked on D_2O. The
526   ^1H chemical shifts of the ^2H, ^{15}N-labelled LpMIP$^{1-213}$, ^{13}C, ^{15}N-labelled LpMIP$^{77-213}$ and ^{13}C, ^{15}N-labelled
527   LpMIP$^{100-213}$ were directly referenced to 3-(trimethylsilyl)propane-1-sulfonate (DSS). ^{13}C and ^{15}N
528   chemical shifts were referenced indirectly to the ^1H DSS standard by the magnetogyric ratio [50].
529   LpMIP$^{1-213}$ was measured in 50mM Tris HCl pH 7, 150 mM NaCl, 0.1 mM DSS, 0.05 % NaN3 and
530   10 % D_2O. Sample conditions for LpMIP$^{77-213}$ and LpMIP$^{100-213}$ were the same except 20 mM Tris HCl
531   pH 7 was used. Final protein concentrations were in the range of 100-150 μM. All spectra were
532   processed using Bruker Topspin 4.1.1 and analyzed using CcpNmr Analysis [51] v2.5 (within the
533   NMRbox virtual environment [52].

534   The previously published NMR backbone assignments of LpMIP$^{1-213}$ (BMRB entry 7021) and LpMIP$^{77-213}$
535   ^{213} (BMRB entry 6334)[37,38] were transferred to our spectra and verified using band-selective excitation
536   short-transient (BEST) transverse relaxation-optimized spectroscopy (TROSY)-based HNCA or
537   HNCACB experiments under our buffer conditions. In contrast, the assignment of LpMIP$^{100-213}$ had to
538   be determined *de novo* by a set of BEST-TROSY-based HN(CA)CO, HNCA and HN(CO)CA, as the
539   ^1H, ^{15}N-HSCQ spectrum of this construct differed significantly from the resonances of the FKBP domain
540   in both LpMIP$^{77-213}$ and full-length LpMIP.

541   Standard NMR pulse sequences implemented in Bruker Topspin library were employed to obtain R_1, R_2
542   and $^{15}N,\{^1H\}$-*NOE* values. For LpMIP$^{1-213}$, TROSY-sampling pulse sequences were used to ensure high
543   data quality. Longitudinal and transverse ^{15}N relaxation rates (R_1 and R_2) of the ^{15}N-^1H bond vectors of
544   backbone amide groups were extracted from signal intensities (I) by a single exponential fit according
545   to equation **1**:

$$I = I_0 e^{-(tR_{1/2})} \qquad (\mathbf{1})$$

547   In R_1 relaxation experiments the variable relaxation delay t was set to 1000 ms, 20 ms, 1500 ms, 60 ms,
548   3000 ms, 100 ms, 800 ms, 200 ms, 40 ms, 400 ms, 80 ms and 600 ms. In all R_2 relaxation experiments
549   the variable loop count was set to 36, 15, 2, 12, 4, 22, 8, 28, 6, 10, 1 and 18. The length of one loop
550   count was 16.96 ms. In the TROSY-based R_2 experiments the loop count length was 8.48 ms. The
551   variable relaxation delay t in R_2 experiments is calculated by length of one loop count times the number
552   of loop counts. The inter-scan delay for the R_1 and R_2 experiments was set to 4 s.

553 The ^{15}N-{^{1}H} steady-state nuclear Overhauser effect measurements ($^{15}N,\{^1H\}$-NOE) were obtained from

554 separate 2D ^{1}H-^{15}N spectra acquired with and without continuous ^{1}H saturation, respectively. The

555 ^{15}N,{^{1}H}-NOE values were determined by taking the ratio of peak volumes from the two spectra,

556 $^{15}N,\{^1H\}$-$NOE = I_{sat}/I_0$, where I_{sat} and I_0 are the peak intensities with and without ^{1}H saturation. The

557 saturation period was approximately $5/R_1$ of the amide protons.

558

559 The averaged ^{1}H and ^{15}N weighted chemical shift perturbations (CSP) observed in ^{1}H, ^{15}N-HSQC

560 spectra were calculated according to equation **2** [53]:

561
$$\text{CSP}=\sqrt{0.5 * \left[\Delta\delta_\text{H}{}^2+(0.15 * \Delta\delta_N)^2\right]} \quad (2)$$

562 Here, $\Delta\delta$H is the ^{1}H chemical shift difference, $\Delta\delta$N is the ^{15}N chemical shift difference, and CSP is the

563 averaged ^{1}H and ^{15}N weighted chemical shift difference in ppm.

564

565 The oligomerization state of a protein can be estimated from the rotational correlation time (τ_c), the time

566 it takes the protein to rotate by one radian under Brownian rotation diffusion. Under the assumption of

567 a spherical globular protein and isotropic motion, τ_c (in ns) can be roughly approximated from the

568 Stokes-Einstein equation (**3**):

569
$$\tau_c = \frac{4\pi\eta r_{eff}{}^3}{3k_BT} \quad (3)$$

570 where η is viscosity (0.89 mPa*s for water at 298.2 K), k_B the Boltzmann constant and T the absolute

571 temperature. The effective hydrodynamic radius r_{eff} can directly be correlated with molecular weight

572 (M_w):

573
$$r_{eff} = \sqrt[3]{\frac{3M_w}{4\pi\rho N_A}} + r_h \quad (4)$$

574 where ρ is the average protein density (1.37 g/cm^3) and N_A the Avogadro constant. For our calculations

575 we used hydration layer radius of 3.2 Å.

576 Based on studies from the Northeast Structural Genomics Consortium an empirical formula could be

577 derived for direct correlation of M_w (in Da) and τ_c (in ns) for proteins in the range of 5-25 kD [40]:

578
$$\tau_c = 0.00062 * M_w - 0.15 \quad (5)$$

579 The rotational correlation time is directly accessible from the ratio of ^{15}N R_1 and R_2 relaxation rates of

580 backbone amide measured at a ^{15}N resonance frequency (v_N) assuming slow isotropic overall motion

581 [40,54] (equation **6**):

582
$$\tau_c = \frac{1}{4\pi v_N}\sqrt{\frac{6R_2}{R_1} - 7} \quad (6)$$

583 **Electron Paramagnetic Resonance (EPR) spectroscopy sample preparation**

584 For spin labelling, Ni-NTA-column-bound single cysteine mutants of LpMIP$^{1-213}$ were incubated

585 overnight at 4 ºC using a 15-fold excess of 3-(2-Iodoacetamido)-2,2,5,5-tetramethyl-1-pyrrolidinyloxy

586 (IPSL) after the washing steps and then purified as described above. Following the IPSL-labelling

17

587   procedure, 4 µL of D_8-glycerol or water was added to a 12 µL of *Lp*MIP sample, mixed thoroughly and

588   gently transferred into a sample tube. The samples for continuous wave EPR were directly measured in

589   a 25 µL micropipettes (BRAND, Germany) with a 0.64-mm diameter at room temperature. Samples for

590   pulsed EPR were flash frozen in liquid nitrogen in a 1.6 mm quartz EPR tube (Suprasil, Wilmad

591   LabGlass) and stored at -80°C.

592

Continuous-wave EPR measurements

594   Continuous-wave (CW) EPR measurements were performed at X-band frequency (9.4 GHz) on a Bruker

595   EMXnano Benchtop Spectrometer at room temperature in a 25 µL micropipette (BRAND, Germany)

596   with a 0.64 mm diameter. The spectra were acquired with 100 kHz modulation frequency, 0.15 mT

597   modulation amplitude, 0.6 - 2 mW microwave power, 5.12 ms time constant, 22.5 ms conversion time,

598   and 18 mT sweep width.

599

Pulsed EPR measurements

601   Pulsed EPR (PELDOR/DEER) experiments were performed on a Bruker Elexsys E580 Q-Band

602   (33.7 GHz) Pulsed ESR spectrometer equipped with an arbitrary waveform generator (SpinJet AWG,

603   Bruker), a 50 W solid state amplifier, a continuous-flow helium cryostat, and a temperature control

604   system (Oxford Instruments). Measurements were performed at 50 K using a $10 - 20$ µL frozen sample

605   containing $15 - 20\%$ glycerol-d_8 in a 1.6 mm quartz ESR tubes (Suprasil, Wilmad LabGlass). For

606   measuring the phase memory times (T_M), a 48 ns $\pi/2$–τ– π Gaussian pulse sequence was used with a

607   two-step phase cycling, while τ was increased in 4 ns steps. PELDOR measurements were performed

608   with a Bruker EN5107D2 dielectric resonator at 50 K using a dead-time free four-pulse sequence and a

609   16-step phase cycling (x [x] [xp]x) [55,56]. A 38 ns Gaussian pulse (full width at half maximum

610   (FWHM) of 16.1 ns) was used as the pump pulse with a 48 ns (FWHM of 20.4 ns) Gaussian observer

611   pulses. The pump pulse was set to the maximum of the echo-detected field swept spectrum and the

612   observer pulses were set at 80 MHz lower. The deuterium modulations were averaged by increasing the

613   first interpulse delay by 16 ns for 8 steps. The five-pulse PELDOR/DEER experiments were performed

614   according to the pulse sequence $\pi/2_{obs} - (\tau/2 - t_0) - \pi_{pump} - t_0 - \pi_{obs} - t' - \pi_{pump} - (\tau - t' + \delta) - \pi_{obs} - (\tau_2$

615   $+ \delta)$. Experiments were performed at 50 K using 48 ns Gaussian observer pulses and a 16-step phase

616   cycling (xx_p [x] [x_p]x). A 36 ns pump pulse was used at $\nu_{obs} + 80$ MHz. Nuclear modulation averaging

617   was performed analogous to 4-pulse PELDOR (16 ns shift in 8 steps) with a corresponding shift of the

618   standing pump pulse. The four-pulse data analysis was performed using Tikhonov regularization as

619   implemented in the MATLAB-based DeerAnalysis2019 package [57]. The background arising from

620   intermolecular interactions were removed from the primary data V(t)/V(0) and the resulting form factors

621   F(t)/F(0) were fitted with a model-free approach to distance distributions. For an error estimation of the

622   probability distribution, the distances for different background functions were determined through

623   gradually changing the time window and the dimensionality for the spin distribution (see Supplementary

624 Table S2). The data was additionally analyzed to predict the distances (and the background) in a user-

625 independent manner using the deep neural network (DEERNet) analysis, which is hosted by the

626 DeerAnalysis2019 package [58,59]. Samples for which both 4-pulse and 5-pulse data are available were

627 globally analyzed using the Python based DeerLab program [60]. Distance distributions for the

628 structures (PDB 8BJC and 1FD9) were simulated using a rotamer library approach using the MATLAB-

629 based MMM2022.2 software package [58].

630

631 **Small angle X-ray scattering (SAXS)**

632 SAXS experiments were carried out at the EMBL-P12 bioSAXS beam line, DESY [61]. SEC-SAXS

633 data were collected [62], $I(q)$ vs q, where $q = 4\pi\sin q/\lambda$ is the scattering angle and λ the X-ray wavelength

634 (0.124 nm; 10 keV). Data collection was carried out at 20 °C using a Superdex200 Increase 5/150

635 analytical SEC column (GE Healthcare) equilibrated in the appropriate buffers (see Table S3) at flow

636 rates of 0.3 mL/min. Automated sample injection and data collection were controlled using the

637 *BECQUEREL* beam line control software [63]. The SAXS intensities were measured from the

638 continuously-flowing column eluent as a continuous series of 0.25 s individual X-ray exposures, using

639 a Pilatus 6M 2D-area detector for a total of one column volume (ca. 600-3000 frames in total, see Table

640 S3). The radial averaging of the data one-dimensional $I(q)$ vs q profiles was carried out with the

641 SASFLOW pipeline incorporating RADAVER from the ATSAS 2.8 software suite [64]. The individual

642 frames obtained for each SEC-SAXS run were processed using CHROMIXS [65]. Briefly, individual

643 SAXS data frames were selected across the respective sample SEC-elution peaks and appropriate solute-

644 free buffer regions of the elution profile were identified, averaged and then subtracted to obtain

645 individual background-subtracted sample data frames. The radius of gyration (R_g) of each data frame

646 was assessed in CHROMIXS and frames with equivalent R_g were scaled and subsequently averaged to

647 produce the final one-dimensional and background-corrected SAXS profiles. Only those scaled

648 individual SAXS data frames with a consistent R_g through the SEC-elution peak that were also evaluated

649 as statistically similar through the measured q-range were included to produce the final SAXS profiles.

650 Corresponding UV traces were not measured; the column eluate was directly moved to the P12 sample

651 exposure unit after the SEC column, forgoing UV absorption measurements, to minimize unwanted

652 band-broadening of the sample. All SAXS data-data comparisons and data-model fits were assessed

653 using the reduced c^2 test and the Correlation Map, or CORMAP, p-value [66]. Fits within the c^2 range

654 of 0.9–1.1 or having CORMAP p-values higher than the significance threshold cutoff of a = 0.01 are

655 considered excellent, i.e., absence of systematic differences between the data-data or data-model fits at

656 the significance threshold.

657 Primary SAXS data were analysed using PRIMUS as well as additional modules from the ATSAS 3.0.1

658 software suite [67]. R_g and the forward scattering at zero angle, $I(0)$ were estimated via the Guinier

659 approximation [68] (ln($I(q)$) vs. q^2 for $qR_g < 1.3$) and the real-space pair distance distribution function,

660 or $p(r)$ profile (calculated from the indirect inverse Fourier transformation of the data, thus also yielding

661   estimates of the maximum particle dimension, D_{max}, Porod volume, V_p, shape classification, and

662   concentration-independent molecular weight [69–71]). Dimensionless Kratky plot representations of the

663   SAXS data ($qR_g^2(I(q)/I(0))$ vs. qR_g) were generated as previously described [72]. All collected SAXS

664   data are reported in Tables S3.

665

666   **Rigid body modeling** – Rigid-body normal mode analysis of LpMIP was performed using the program

667   SREFLEX [73] using the LpMIP apo and JK095-bound X-ray crystal structures (PDB: 1FD9, 8BJD and

668   8BJC) as templates. CRYSOL was used to assess data-model fits [74].

669

670   **Thermal stability assay**

671   10 µg of purified LpMIP constructs in 20mM Tris pH 7, 150 mM NaCl were incubated with a final

672   concentration of 0.02% DMSO or a 5-fold molar excess of JK095 in DMSO (0.02% final concentration).

673   2.5 µL of a 50x SYPRO Orange (Merck) stock was added to each sample directly before measurement

674   of the melting temperature in a 96-well plate on a QuantStudio 1 Real-Time PCR System reader (Thermo

675   Fisher) with a temperature increase of 0.05 °C/min. The fluorescence of SYPRO Orange was measured

676   using the filter calibrated for SYBR GREEN with an excitation filter of 470 ± 15 nm and an emission

677   filter of 520 ± 15 nm.

678

679   **Data availability**

680   The coordinates of the refined models and structure factors have been deposited into the PDB repository:

681   8BJC for LpMIP[1-213], 8BJD for LpMIP[1-213]JK095, 8BK6 for LpMIP[100-213] JK095, 8BK5 for LpMIP[77-213]

682   JK095, 8BJE for LpMIP[77-213] JK236 and 8BK4 for TcMIP JK236. The NMR backbone assignment of

683   LpMIP[100-213] has been deposited in the BioMagResBank (www.bmrb.io) under the accession number

684   51861. The NMR backbone assignments for full-length LpMIP[1-213] and LpMIP[77-213] are available from

685   the BMRB under the accession numbers 7021 and 6334, respectively [38,75]. SAXS data for full-length

686   LpMIP have been deposited in the SASBDB under the accession numbers SASXXX, SASXXX and

687   SASXXX.

688

689   **Conflict of interest**

690   The authors have no conflict of interest to declare.

691

692   **Author contributions**

693   Sample preparation: CW, VHPC, FT, BG; Biochemistry: VHCP, FT, BG; X-ray crystallography: JJW,

694   BG, AG; NMR spectroscopy: CW, VHPC, FT, BG; EPR spectroscopy: VHPC, MD, BJ; SAXS: CW,

695   FT, BG, JMH; Inhibitor synthesis: PK; Conceptualization: UAH; Funding acquisition: FH, AG, UAH;

696   Supervision: BG, FH, AG, UAH; Paper writing – first draft: UAH; Paper writing – review and editing:

697 CW, JJW, BG, BJ, AG, UAH; visualization: CW, JJW, VHPC, MD, BG, UAH. All authors read and
698 approved the final version of the manuscript.
699

References

[1] J.E. Martyn, L. Gomez-Valero, C. Buchrieser, The evolution and role of eukaryotic-like domains in environmental intracellular bacteria: the battle with a eukaryotic cell, FEMS Microbiology Reviews. 46 (2022) fuac012. https://doi.org/10.1093/femsre/fuac012.

[2] I.G. Gonçalves, L.C. Simões, M. Simões, Legionella pneumophila, Trends in Microbiology. 29 (2021) 860–861. https://doi.org/10.1016/j.tim.2021.04.005.

[3] C.M. Anand, A.R. Skinner, A. Malic, J.B. Kurtz, Interaction of L. pneumophilia and a free living amoeba (Acanthamoeba palestinensis)., J Hyg (Lond). 91 (1983) 167–178.

[4] D. Chauhan, S.R. Shames, Pathogenicity and Virulence of Legionella: Intracellular replication and host response, Virulence. 12 (n.d.) 1122–1144. https://doi.org/10.1080/21505594.2021.1903199.

[5] M.F. Brady, V. Sundareshan, Legionnaires' Disease, in: StatPearls, StatPearls Publishing, Treasure Island (FL), 2022. http://www.ncbi.nlm.nih.gov/books/NBK430807/ (accessed November 20, 2022).

[6] D. Viasus, V. Gaia, C. Manzur-Barbur, J. Carratalà, Legionnaires' Disease: Update on Diagnosis and Treatment, Infect Dis Ther. 11 (2022) 973–986. https://doi.org/10.1007/s40121-022-00635-7.

[7] J. Hacker, M. Ott, E. Wintermeyer, B. Ludwig, G. Fischer, Analysis of virulence factors of Legionella pneumophila, Zentralbl Bakteriol. 278 (1993) 348–358. https://doi.org/10.1016/s0934-8840(11)80851-0.

[8] N.C. Engleberg, C. Carter, D.R. Weber, N.P. Cianciotto, B.I. Eisenstein, DNA sequence of mip, a Legionella pneumophila gene associated with macrophage infectivity, Infect Immun. 57 (1989) 1263–1270. https://doi.org/10.1128/iai.57.4.1263-1270.1989.

[9] N.P. Cianciotto, B.I. Eisenstein, C.H. Mody, G.B. Toews, N.C. Engleberg, A Legionella pneumophila gene encoding a species-specific surface protein potentiates initiation of intracellular infection, Infect Immun. 57 (1989) 1255–1262. https://doi.org/10.1128/iai.57.4.1255-1262.1989.

[10] N.P. Cianciotto, B.I. Eisenstein, C.H. Mody, N.C. Engleberg, A mutation in the mip gene results in an attenuation of Legionella pneumophila virulence, J Infect Dis. 162 (1990) 121–126. https://doi.org/10.1093/infdis/162.1.121.

[11] J. Rasch, C.M. Ünal, A. Klages, Ü. Karsli, N. Heinsohn, R.M.H.J. Brouwer, M. Richter, A. Dellmann, M. Steinert, Peptidyl-Prolyl-cis/trans-Isomerases Mip and PpiB of Legionella pneumophila Contribute to Surface Translocation, Growth at Suboptimal Temperature, and Infection, Infect Immun. 87 (2018) e00939-17. https://doi.org/10.1128/IAI.00939-17.

[12] N.P. Cianciotto, B.S. Fields, Legionella pneumophila mip gene potentiates intracellular infection of protozoa and human macrophages, Proc Natl Acad Sci U S A. 89 (1992) 5188–5191. https://doi.org/10.1073/pnas.89.11.5188.

[13] B. Schmidt, J. Rahfeld, A. Schierhorn, B. Ludwig, J. Hacker, G. Fischer, A homodimer represents an active species of the peptidyl-prolyl cis/trans isomerase FKBP25mem from Legionella pneumophila, FEBS Lett. 352 (1994) 185–190. https://doi.org/10.1016/0014-5793(94)00970-8.

[14] A. Riboldi-Tunnicliffe, B. König, S. Jessen, M.S. Weiss, J. Rahfeld, J. Hacker, G. Fischer, R. Hilgenfeld, Crystal structure of Mip, a prolylisomerase from Legionella pneumophila, Nat Struct Mol Biol. 8 (2001) 779–783. https://doi.org/10.1038/nsb0901-779.

[15] G. Fischer, H. Bang, B. Ludwig, K. Mann, J. Hacker, Mip protein of Legionella pneumophila exhibits peptidyl-prolyl-cis/trans isomerase (PPIase) activity, Molecular Microbiology. 6 (1992) 1375–1383. https://doi.org/10.1111/j.1365-2958.1992.tb00858.x.

[16] M.W. Harding, A. Galat, D.E. Uehling, S.L. Schreiber, A receptor for the immuno-suppressant FK506 is a cis–trans peptidyl-prolyl isomerase, Nature. 341 (1989) 758–760. https://doi.org/10.1038/341758a0.

[17] J.J. Siekierka, S.H.Y. Hung, M. Poe, C.S. Lin, N.H. Sigal, A cytosolic binding protein for the immunosuppressant FK506 has peptidyl-prolyl isomerase activity but is distinct from cyclophilin, Nature. 341 (1989) 755–757. https://doi.org/10.1038/341755a0.

[18] C.B. Kang, Y. Hong, S. Dhe-Paganon, H.S. Yoon, FKBP family proteins: immunophilins with versatile biological functions, Neurosignals. 16 (2008) 318–325. https://doi.org/10.1159/000123041.

[19] C. Ünal, K.F. Schwedhelm, A. Thiele, M. Weiwad, K. Schweimer, F. Frese, G. Fischer, J. Hacker, C. Faber, M. Steinert, Collagen IV-derived peptide binds hydrophobic cavity of Legionella pneumophila Mip and interferes with bacterial epithelial transmigration, Cellular Microbiology. 13 (2011) 1558–1572. https://doi.org/10.1111/j.1462-5822.2011.01641.x.

[20] C. Wagner, A.S. Khan, T. Kamphausen, B. Schmausser, C. Ünal, U. Lorenz, G. Fischer, J. Hacker, M. Steinert, Collagen binding protein Mip enables Legionella pneumophila to transmigrate through a barrier of NCI-H292 lung epithelial cells and extracellular matrix, Cellular Microbiology. 9 (2007) 450–462. https://doi.org/10.1111/j.1462-5822.2006.00802.x.

[21] A. Ceymann, M. Horstmann, P. Ehses, K. Schweimer, A.-K. Paschke, M. Steinert, C. Faber, Solution structure of the Legionella pneumophila Mip-rapamycin complex, BMC Struct Biol. 8 (2008) 17. https://doi.org/10.1186/1472-6807-8-17.

[22] A.G. Lundemose, S. Birkelund, S.J. Fey, P.M. Larsen, G. Christiansen, Chlamydia trachomatis contains a protein similar to the Legionella pneumophila mip gene product, Mol Microbiol. 5 (1991) 109–115. https://doi.org/10.1111/j.1365-2958.1991.tb01831.x.

[23] R. Leuzzi, L. Serino, M. Scarselli, S. Savino, M.R. Fontana, E. Monaci, A. Taddei, G. Fischer, R. Rappuoli, M. Pizza, Ng-MIP, a surface-exposed lipoprotein of Neisseria gonorrhoeae, has a peptidyl-prolyl cis/trans isomerase (PPIase) activity and is involved in persistence in macrophages, Mol Microbiol. 58 (2005) 669–681. https://doi.org/10.1111/j.1365-2958.2005.04859.x.

[24] S.M. Horne, T.J. Kottom, L.K. Nolan, K.D. Young, Decreased intracellular survival of an fkpA mutant of Salmonella typhimurium Copenhagen, Infect Immun. 65 (1997) 806–810. https://doi.org/10.1128/iai.65.2.806-810.1997.

[25] Q. Huang, J. Yang, C. Li, Y. Song, Y. Zhu, N. Zhao, X. Mou, X. Tang, G. Luo, A. Tong, B. Sun, H. Tang, H. Li, L. Bai, R. Bao, Structural characterization of PaFkbA: A periplasmic chaperone from Pseudomonas aeruginosa, Computational and Structural Biotechnology Journal. 19 (2021) 2460–2467. https://doi.org/10.1016/j.csbj.2021.04.045.

[26] P.J.B. Pereira, M.C. Vega, E. González-Rey, R. Fernández-Carazo, S. Macedo-Ribeiro, F.X. Gomis-Rüth, A. González, M. Coll, Trypanosoma cruzi macrophage infectivity potentiator has a rotamase core and a highly exposed α-helix, EMBO Reports. 3 (2002) 88–94. https://doi.org/10.1093/embo-reports/kvf009.

[27] A. Moro, F. Ruiz-Cabello, A. Fernández-Cano, R.P. Stock, A. González, Secretion by Trypanosoma cruzi of a peptidyl-prolyl cis-trans isomerase involved in cell infection., EMBO J. 14 (1995) 2483–2490.

[28] L.M.D. Magalhães, K.J. Gollob, B. Zingales, W.O. Dutra, Pathogen diversity, immunity, and the fate of infections: lessons learned from Trypanosoma cruzi human-host interactions, Lancet Microbe. 3 (2022) e711–e722. https://doi.org/10.1016/S2666-5247(21)00265-2.

[29] C.M. Ünal, M. Steinert, Microbial peptidyl-prolyl cis/trans isomerases (PPIases): virulence factors and potential alternative drug targets, Microbiol Mol Biol Rev. 78 (2014) 544–571. https://doi.org/10.1128/MMBR.00015-14.

[30] J.M. Kolos, A.M. Voll, M. Bauder, F. Hausch, FKBP Ligands-Where We Are and Where to Go?, Front Pharmacol. 9 (2018) 1425. https://doi.org/10.3389/fphar.2018.01425.

[31] N.J. Scheuplein, N.M. Bzdyl, E.A. Kibble, T. Lohr, U. Holzgrabe, M. Sarkar-Tyson, Targeting Protein Folding: A Novel Approach for the Treatment of Pathogenic Bacteria, J Med Chem. 63 (2020) 13355–13388. https://doi.org/10.1021/acs.jmedchem.0c00911.

[32] I.H. Norville, N.J. Harmer, S.V. Harding, G. Fischer, K.E. Keith, K.A. Brown, M. Sarkar-Tyson, R.W. Titball, A Burkholderia pseudomallei Macrophage Infectivity Potentiator-Like Protein Has Rapamycin-Inhibitable Peptidy*Lp*rolyl Isomerase Activity and Pleiotropic Effects on Virulence ▽, Infect Immun. 79 (2011) 4299–4307. https://doi.org/10.1128/IAI.00134-11.

820 [33] I.H. Norville, K. O'Shea, M. Sarkar-Tyson, S. Zheng, R.W. Titball, G. Varani, N.J. Harmer, The
821   structure of a *Burkholderia pseudomallei* immunophilin–inhibitor complex reveals new
822   approaches to antimicrobial development, Biochemical Journal. 437 (2011) 413–422.
823   https://doi.org/10.1042/BJ20110345.
824 [34] S. Pomplun, C. Sippel, A. Hähle, D. Tay, K. Shima, A. Klages, C.M. Ünal, B. Rieß, H.T. Toh, G.
825   Hansen, H.S. Yoon, A. Bracher, P. Preiser, J. Rupp, M. Steinert, F. Hausch, Chemogenomic
826   Profiling of Human and Microbial FK506-Binding Proteins, J Med Chem. 61 (2018) 3660–3673.
827   https://doi.org/10.1021/acs.jmedchem.8b00137.
828 [35] C.M. Ünal, M. Steinert, FKBPs in bacterial infections, Biochim Biophys Acta. 1850 (2015) 2096–
829   2102. https://doi.org/10.1016/j.bbagen.2014.12.018.
830 [36] S. Khan, S. Khan, S. Baboota, J. Ali, Immunosuppressive drug therapy – biopharmaceutical
831   challenges and remedies, Expert Opinion on Drug Delivery. 12 (2015) 1333–1349.
832   https://doi.org/10.1517/17425247.2015.1005072.
833 [37] M.V. Petoukhov, D.I. Svergun, Global Rigid Body Modeling of Macromolecular Complexes
834   against Small-Angle Scattering Data, Biophysical Journal. 89 (2005) 1237–1250.
835   https://doi.org/10.1529/biophysj.105.064154.
836 [38] M. Horstmann, T. Kamphausen, K. Schweimer, M. Steinert, J. Hacker, A. Haase, P. Rösch, G.
837   Schweimer, C. Faber, Letter to the Editor: 1H, 13C, 15N backbone and sidechain resonance
838   assignment of Mip(77–213) the PPIase domain of the Legionella pneumophila Mip protein, J
839   Biomol NMR. 31 (2005) 77–78. https://doi.org/10.1007/s10858-004-6041-6.
840 [39] R. Deutscher, S. Karagöz, P. Purder, J. Kolos, C. Meyners, W. Sugiarto, P. Krajczy, F. Tebbe, T.
841   Geiger, C. Ünal, U. Hellmich, M. Steinert, F. Hausch, [4.3.1] Bicyclic FKBP ligands inhibit
842   Legionella pneumophila infection by *Lp*Mip-dependent and *Lp*Mip independent mechanisms,
843   (2023). https://doi.org/10.26434/chemrxiv-2023-vfssm.
844 [40] P. Rossi, G.V.T. Swapna, Y.J. Huang, J.M. Aramini, C. Anklin, K. Conover, K. Hamilton, R. Xiao,
845   T.B. Acton, A. Ertekin, J.K. Everett, G.T. Montelione, A microscale protein NMR sample
846   screening pipeline, J Biomol NMR. 46 (2010) 11–22. https://doi.org/10.1007/s10858-009-9386-
847   z.
848 [41] J.M. Kolos, S. Pomplun, S. Jung, B. Rieß, P.L. Purder, A.M. Voll, S. Merz, M. Gnatzy, T.M. Geiger,
849   I. Quist-Løkken, J. Jatzlau, P. Knaus, T. Holien, A. Bracher, C. Meyners, P. Czodrowski, V.
850   Krewald, F. Hausch, Picomolar FKBP inhibitors enabled by a single water-displacing methyl
851   group in bicyclic [4.3.1] aza-amides, Chem. Sci. 12 (2021) 14758–14765.
852   https://doi.org/10.1039/D1SC04638A.
853 [42] K. Hu, V. Galius, K. Pervushin, Structural Plasticity of Peptidyl–Prolyl Isomerase sFkpA Is a Key to
854   Its Chaperone Function As Revealed by Solution NMR, Biochemistry. 45 (2006) 11983–11991.
855   https://doi.org/10.1021/bi0607913.
856 [43] R.B. Best, K. Lindorff-Larsen, M.A. DePristo, M. Vendruscolo, Relation between native
857   ensembles and experimental structures of proteins, Proceedings of the National Academy of
858   Sciences. 103 (2006) 10901–10906. https://doi.org/10.1073/pnas.0511156103.
859 [44] P.K.A. Jagtap, S. Asami, C. Sippel, V.R.I. Kaila, F. Hausch, M. Sattler, Selective Inhibitors of
860   FKBP51 Employ Conformational Selection of Dynamic Invisible States, Angewandte Chemie
861   International Edition. 58 (2019) 9429–9433. https://doi.org/10.1002/anie.201902994.
862 [45] W. Kabsch, Integration, scaling, space-group assignment and post-refinement, Acta Cryst D. 66
863   (2010) 133–144. https://doi.org/10.1107/S0907444909047374.
864 [46] A.J. McCoy, R.W. Grosse-Kunstleve, P.D. Adams, M.D. Winn, L.C. Storoni, R.J. Read, Phaser
865   crystallographic software, J Appl Cryst. 40 (2007) 658–674.
866   https://doi.org/10.1107/S0021889807021206.
867 [47] P. Emsley, B. Lohkamp, W.G. Scott, K. Cowtan, Features and development of Coot, Acta Cryst D.
868   66 (2010) 486–501. https://doi.org/10.1107/S0907444910007493.
869 [48] G.N. Murshudov, A.A. Vagin, E.J. Dodson, Refinement of Macromolecular Structures by the
870   Maximum-Likelihood Method, Acta Cryst D. 53 (1997) 240–255.
871   https://doi.org/10.1107/S0907444996012255.

872 [49] E.F. Pettersen, T.D. Goddard, C.C. Huang, E.C. Meng, G.S. Couch, T.I. Croll, J.H. Morris, T.E.
873   Ferrin, UCSF ChimeraX: Structure visualization for researchers, educators, and developers,
874   Protein Science. 30 (2021) 70–82. https://doi.org/10.1002/pro.3943.

875 [50] D.S. Wishart, C.G. Bigam, J. Yao, F. Abildgaard, H.J. Dyson, E. Oldfield, J.L. Markley, B.D. Sykes,
876   1H, 13C and 15N chemical shift referencing in biomolecular NMR, J Biomol NMR. 6 (1995) 135–
877   140. https://doi.org/10.1007/BF00211777.

878 [51] W.F. Vranken, W. Boucher, T.J. Stevens, R.H. Fogh, A. Pajon, M. Llinas, E.L. Ulrich, J.L. Markley,
879   J. Ionides, E.D. Laue, The CCPN data model for NMR spectroscopy: Development of a software
880   pipeline, Proteins: Structure, Function, and Bioinformatics. 59 (2005) 687–696.
881   https://doi.org/10.1002/prot.20449.

882 [52] M.W. Maciejewski, A.D. Schuyler, M.R. Gryk, I.I. Moraru, P.R. Romero, E.L. Ulrich, H.R.
883   Eghbalnia, M. Livny, F. Delaglio, J.C. Hoch, NMRbox: A Resource for Biomolecular NMR
884   Computation, Biophysical Journal. 112 (2017) 1529–1534.
885   https://doi.org/10.1016/j.bpj.2017.03.011.

886 [53] M.P. Williamson, Using chemical shift perturbation to characterise ligand binding, Prog Nucl
887   Magn Reson Spectrosc. 73 (2013) 1–16. https://doi.org/10.1016/j.pnmrs.2013.02.001.

888 [54] L.E. Kay, D.A. Torchia, A. Bax, Backbone dynamics of proteins as studied by nitrogen-15 inverse
889   detected heteronuclear NMR spectroscopy: application to staphylococcal nuclease,
890   Biochemistry. 28 (1989) 8972–8979. https://doi.org/10.1021/bi00449a003.

891 [55] M. Pannier, S. Veit, A. Godt, G. Jeschke, H.W. Spiess, Dead-Time Free Measurement of Dipole–
892   Dipole Interactions between Electron Spins, Journal of Magnetic Resonance. 142 (2000) 331–
893   340. https://doi.org/10.1006/jmre.1999.1944.

894 [56] C.E. Tait, S. Stoll, Coherent pump pulses in Double Electron Electron Resonance spectroscopy,
895   Phys. Chem. Chem. Phys. 18 (2016) 18470–18485. https://doi.org/10.1039/C6CP03555H.

896 [57] G. Jeschke, V. Chechik, P. Ionita, A. Godt, H. Zimmermann, J. Banham, C.R. Timmel, D. Hilger, H.
897   Jung, DeerAnalysis2006—a comprehensive software package for analyzing pulsed ELDOR data,
898   Appl. Magn. Reson. 30 (2006) 473–498. https://doi.org/10.1007/BF03166213.

899 [58] Y. Polyhach, E. Bordignon, G. Jeschke, Rotamer libraries of spin labelled cysteines for protein
900   studies, Phys. Chem. Chem. Phys. 13 (2011) 2356–2366. https://doi.org/10.1039/C0CP01865A.

901 [59] S.G. Worswick, J.A. Spencer, G. Jeschke, I. Kuprov, Deep neural network processing of DEER
902   data, Science Advances. 4 (2018) eaat5218. https://doi.org/10.1126/sciadv.aat5218.

903 [60] L. Fábregas Ibáñez, G. Jeschke, S. Stoll, DeerLab: a comprehensive software package for
904   analyzing dipolar electron paramagnetic resonance spectroscopy data, Magnetic Resonance. 1
905   (2020) 209–224. https://doi.org/10.5194/mr-1-209-2020.

906 [61] C.E. Blanchet, A. Spilotros, F. Schwemmer, M.A. Graewert, A. Kikhney, C.M. Jeffries, D. Franke,
907   D. Mark, R. Zengerle, F. Cipriani, S. Fiedler, M. Roessle, D.I. Svergun, Versatile sample
908   environments and automation for biological solution X-ray scattering experiments at the P12
909   beamline (PETRA III, DESY), J Appl Cryst. 48 (2015) 431–443.
910   https://doi.org/10.1107/S160057671500254X.

911 [62] M.A. Graewert, S. Da Vela, T.W. Gräwert, D.S. Molodenskiy, C.E. Blanchet, D.I. Svergun, C.M.
912   Jeffries, Adding Size Exclusion Chromatography (SEC) and Light Scattering (LS) Devices to Obtain
913   High-Quality Small Angle X-Ray Scattering (SAXS) Data, Crystals. 10 (2020) 975.
914   https://doi.org/10.3390/cryst10110975.

915 [63] N.R. Hajizadeh, D. Franke, D.I. Svergun, Integrated beamline control and data acquisition for
916   small-angle X-ray scattering at the P12 BioSAXS beamline at PETRAIII storage ring DESY, J
917   Synchrotron Rad. 25 (2018) 906–914. https://doi.org/10.1107/S1600577518005398.

918 [64] D. Franke, A.G. Kikhney, D.I. Svergun, Automated acquisition and analysis of small angle X-ray
919   scattering data, Nuclear Instruments and Methods in Physics Research Section A: Accelerators,
920   Spectrometers, Detectors and Associated Equipment. 689 (2012) 52–59.
921   https://doi.org/10.1016/j.nima.2012.06.008.

[65] A. Panjkovich, D.I. Svergun, CHROMIXS: automatic and interactive analysis of chromatography-coupled small-angle X-ray scattering data, Bioinformatics. 34 (2018) 1944–1946. https://doi.org/10.1093/bioinformatics/btx846.

[66] D. Franke, C.M. Jeffries, D.I. Svergun, Correlation Map, a goodness-of-fit test for one-dimensional X-ray scattering spectra, Nat Methods. 12 (2015) 419–422. https://doi.org/10.1038/nmeth.3358.

[67] K. Manalastas-Cantos, P.V. Konarev, N.R. Hajizadeh, A.G. Kikhney, M.V. Petoukhov, D.S. Molodenskiy, A. Panjkovich, H.D.T. Mertens, A. Gruzinov, C. Borges, C.M. Jeffries, D.I. Svergun, D. Franke, ATSAS 3.0: expanded functionality and new tools for small-angle scattering data analysis, J Appl Cryst. 54 (2021) 343–355. https://doi.org/10.1107/S1600576720013412.

[68] A. Guinier, La diffraction des rayons X aux très petits angles : application à l'étude de phénomènes ultramicroscopiques, Ann. Phys. 11 (1939) 161–237. https://doi.org/10.1051/anphys/193911120161.

[69] D.I. Svergun, Determination of the regularization parameter in indirect-transform methods using perceptual criteria, J Appl Cryst. 25 (1992) 495–503. https://doi.org/10.1107/S0021889892001663.

[70] N.R. Hajizadeh, D. Franke, C.M. Jeffries, D.I. Svergun, Consensus Bayesian assessment of protein molecular mass from solution X-ray scattering data, Sci Rep. 8 (2018) 7204. https://doi.org/10.1038/s41598-018-25355-2.

[71] D. Franke, C.M. Jeffries, D.I. Svergun, Machine Learning Methods for X-Ray Scattering Data Analysis from Biomacromolecular Solutions, Biophysical Journal. 114 (2018) 2485–2492. https://doi.org/10.1016/j.bpj.2018.04.018.

[72] V. Receveur-Brechot, D. Durand, How random are intrinsically disordered proteins? A small angle scattering perspective, Curr Protein Pept Sci. 13 (2012) 55–75. https://doi.org/10.2174/138920312799277901.

[73] A. Panjkovich, D.I. Svergun, Deciphering conformational transitions of proteins by small angle X-ray scattering and normal mode analysis, Phys. Chem. Chem. Phys. 18 (2016) 5707–5719. https://doi.org/10.1039/C5CP04540A.

[74] D. Svergun, C. Barberato, M.H.J. Koch, CRYSOL – a Program to Evaluate X-ray Solution Scattering of Biological Macromolecules from Atomic Coordinates, J Appl Cryst. 28 (1995) 768–773. https://doi.org/10.1107/S0021889895007047.

[75] M. Horstmann, P. Ehses, K. Schweimer, M. Steinert, T. Kamphausen, G. Fischer, J. Hacker, P. Rösch, C. Faber, Domain Motions of the Mip Protein from Legionella pneumophila, Biochemistry. 45 (2006) 12303–12311. https://doi.org/10.1021/bi060818i.
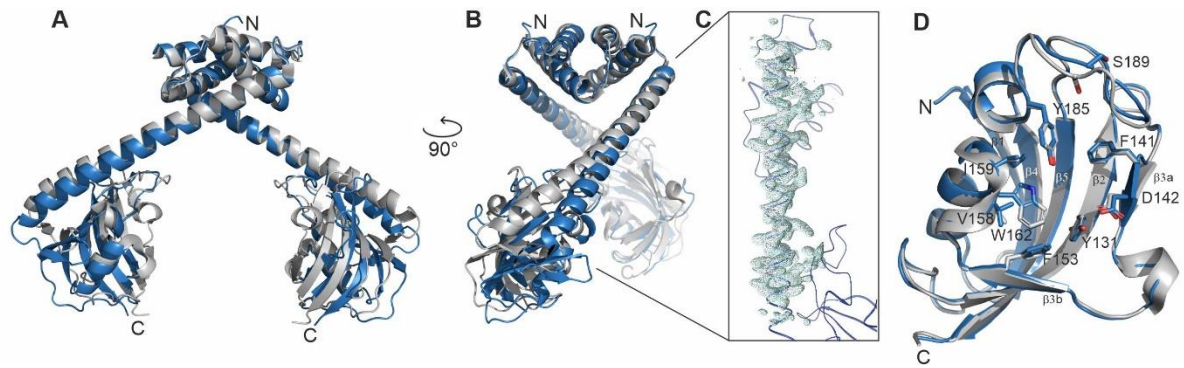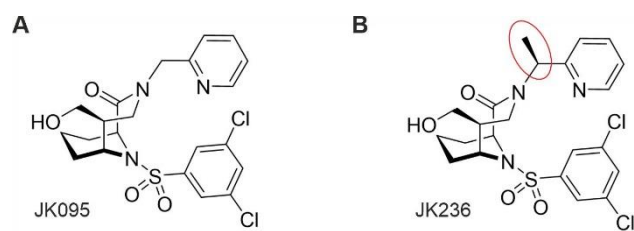
Fig. 1: Comparison of full-length *Lp*MIP structures reveal stalk helix splaying.

(**A, B**) Overlay of the N-terminal dimerization domains of the two currently available *Lp*MIP[1-213] structures (PDB: 1FD9 at 2.41 Å, grey; PDB: 8BJC at 1.71 Å, blue) shows ~18° stalk helix splaying.

(**C**) Importantly, the stalk helix backbone of our newly determined *Lp*MIP structure (blue) can be unambiguously placed in the 2Fo–Fc electron density map, shown here as a light blue mesh at 3σ. For clarity, only the density map for the stalk helix backbone is shown.

(**D**) Overlay of the FKBP-like domains from the two *Lp*MIP structures. Residues surrounding the active site are shown as sticks, β-strands are labeled.

Scheme 1: [**4.3.1]-aza-bicyclic sulfonamide inhibitors used in this study.** JK095 (**A**) and JK236 (**B**) differ by the insertion of a stereospecific methyl group in the pyridine linker.
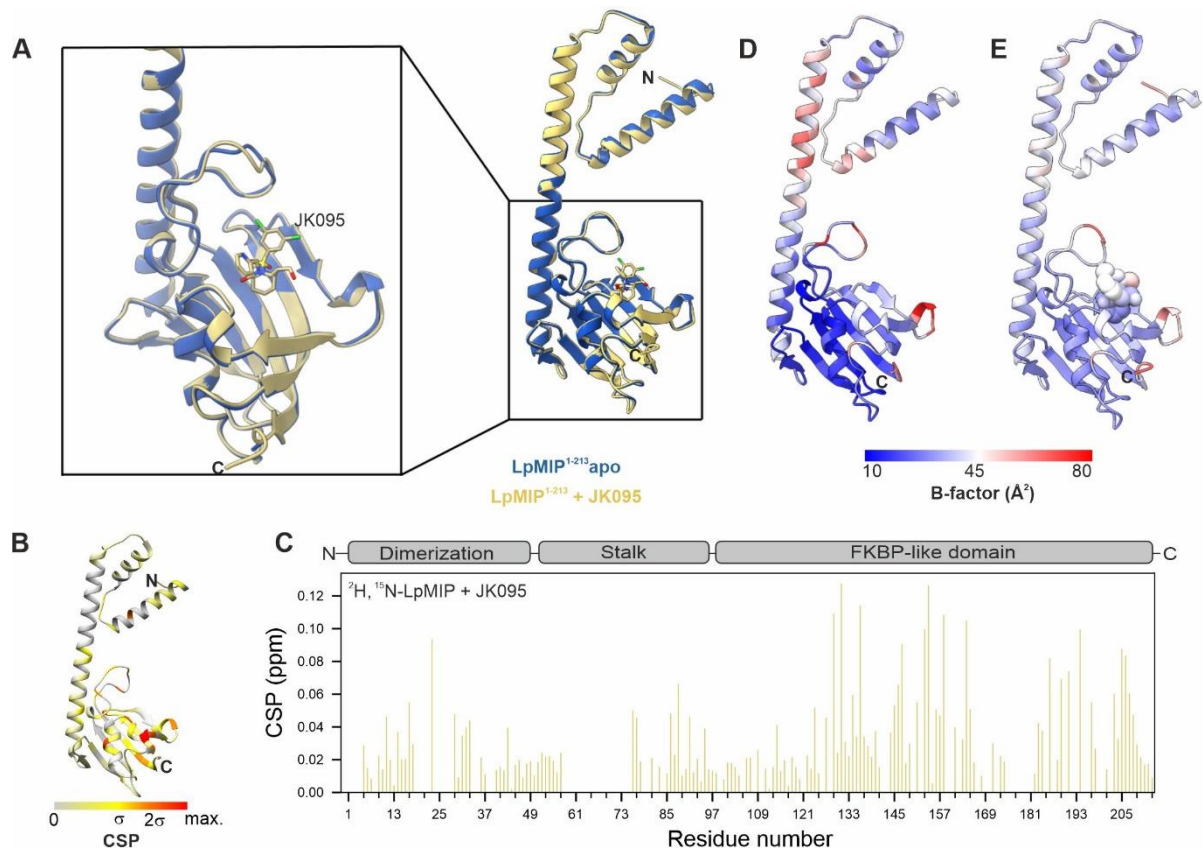
Fig. 2: Comparison of full-length *Lp*MIP in the absence and presence of a bicyclic inhibitor.

(**A**) Overlay of *Lp*MIP in the absence (blue, PDB: 8BJC) and presence of JK095 (yellow, PDB: 8BJD). The two structures align with a backbone RMSD of 0.349 Å. In the zoom of the FKBP-like domain, JK095 is shown as sticks. Non-carbon atom color scheme: blue: N, red: O, yellow: S, green: Cl. Note that the orientation of the zoom has been slightly tilted to better visualize the structural differences in the β4/β5-loop.

(**B, C**) Chemical shift changes in ^{2}H, ^{15}N-labeled *Lp*MIP titrated with JK095 mapped on the *Lp*MIP crystal structure (B) and per residue (C) with the protein topology shown on top for orientation.

(**D, E**) Crystallographic B-factors of *Lp*MIP in the absence (D) and presence (E) of JK095.
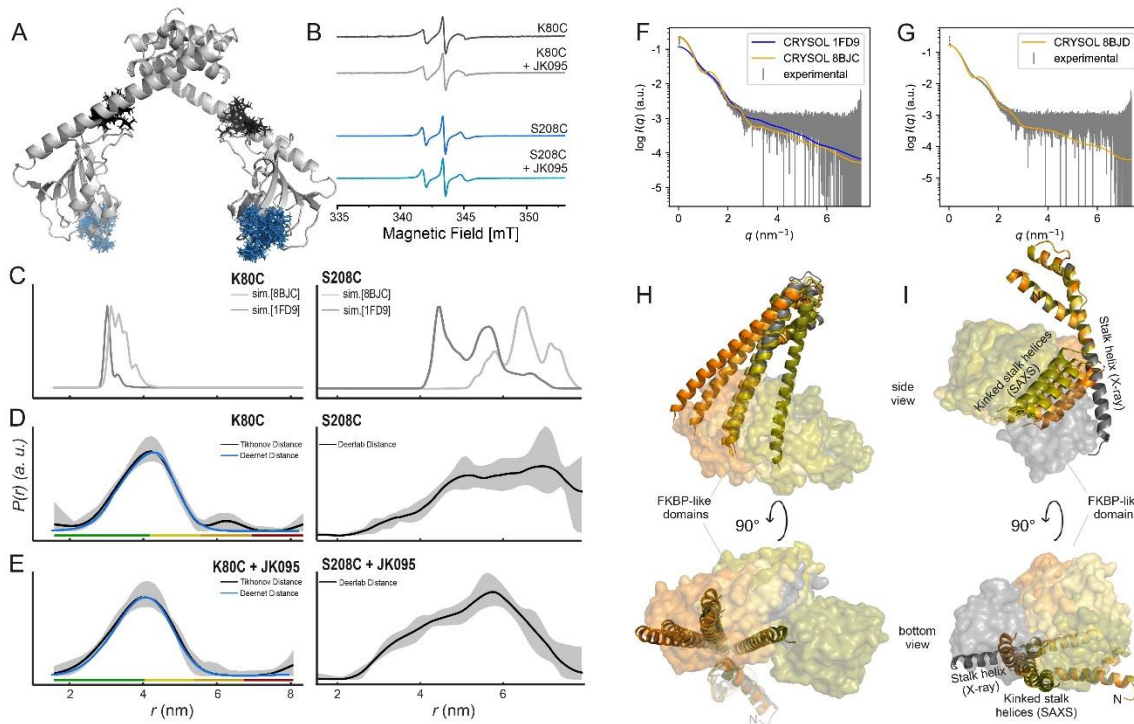
Fig. 3: Structural dynamics of full-length *Lp*MIP in solution.

(**A**) Simulated rotamers of proxyl-spin labels attached to *Lp*MIP at position K80C (black) or S208C (teal) (on PDB: 8BJC using MATLAB-based MMM2022.2 software).

(**B**) Continuous-wave EPR spectra of spin-labeled *Lp*MIP single-cysteine variants.

(**C**) Predicted interspin distances (sim.) for *Lp*MIP K80C (left) and *Lp*MIP S208C (right) based on the available *apo* state crystal structures (PDB-IDs: 8BJC, 1FD9). (**D, E**) Measured spin label distances using PELDOR/DEER spectroscopy in the absence (D) and presence (E) of JK095. For *Lp*MIP S208C, distances were determined through a global analysis of 4-pulse and 5-pulse PELDOR data (see Fig. S5). The rainbow code at the bottom indicates reliability for the probability distribution. (Green: shape, width and mean reliable; yellow: width and mean reliable, orange: mean reliable; red: not reliable) (**F, G**) SAXS scattering data for *Lp*MIP in the absence (F) and presence of JK095 (G). The simulated scattering curves (orange and blue traces) based on the available X-ray structures of *apo Lp*MIP (PDB: 8BJC, 1F9J) or with JK095 (PDB: 8BJD) does not match the scattering profile of the protein in solution after least-square fit to experimental values for 0.5 nm^{-1}< q <1.5 nm^{-1}.

(**H, I**) For a better fit with the experimental SAXS data of *Lp*MIP in solution, SREFLEX modeling was carried out. This yields *Lp*MIP structural models with straight (H) and kinked (I) stalk helices. Accordingly, also the relative orientation of the FKBP like domains (shown as transparent surfaces) changes dramatically. The X-ray structure (PBD: 8BJC) is shown in grey, representative SREFLEX models in orange hues. For better visualization, models with straight and kinked helices are shown in separate chains. There are no discernible differences between the *apo* and JK095-bound state in the *Lp*MIP SREFLEX models, thus only the *apo* models are shown (for details see main text).
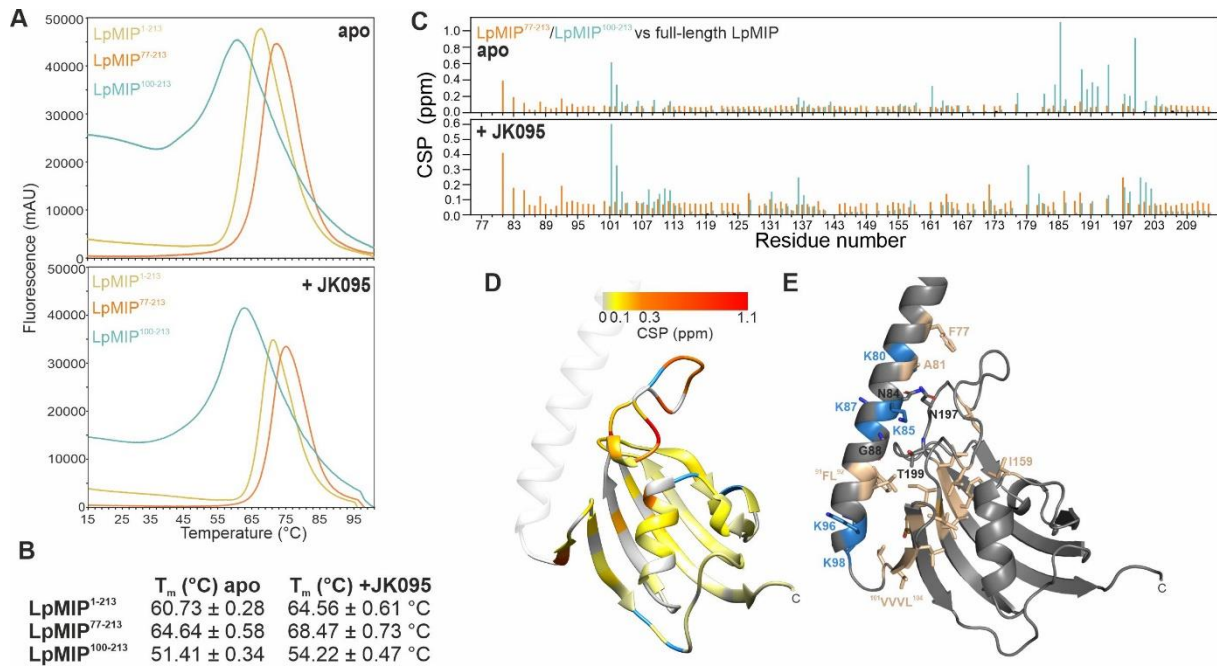
Fig. 4: Role of the *Lp*MIP appendage domains for protein stability and crosstalk with the FKBP-like domain.

(**A**) Fluorescence-based melting assay. The melting temperature (T_m) for full-length *Lp*MIP (yellow) or two deletion constructs (orange, cyan) in the absence (top) or presence of a three-fold molar excess of JK095 (bottom) can be obtained from the inversion point of the upward slope.

(**B**) T_m values for the three constructs obtained from the curves shown in (A). Errors are standard deviations from three replicates.

(**C**) Chemical shift perturbations of the FKBP-like domain resonances of *Lp*MIP[77-213] and *Lp*MIP[100-213] compared to full-length *Lp*MIP (orange and blue, respectively) in the *apo* state (top) and with JK095 (bottom). (**D**) Chemical shift differences between full-length *Lp*MIP and *Lp*MIP[100-213] mapped on the FKBP-like domain, residues for which no signal is observed in *Lp*MIP[100-213] are colored blue.

(**E**) Details of hydrophobic interaction network between stalk helix and FKBP-like domain. Hydrophobic residues shown in sand, basic residues in blue, all others in grey. For a better overview, not all sidechains are shown.
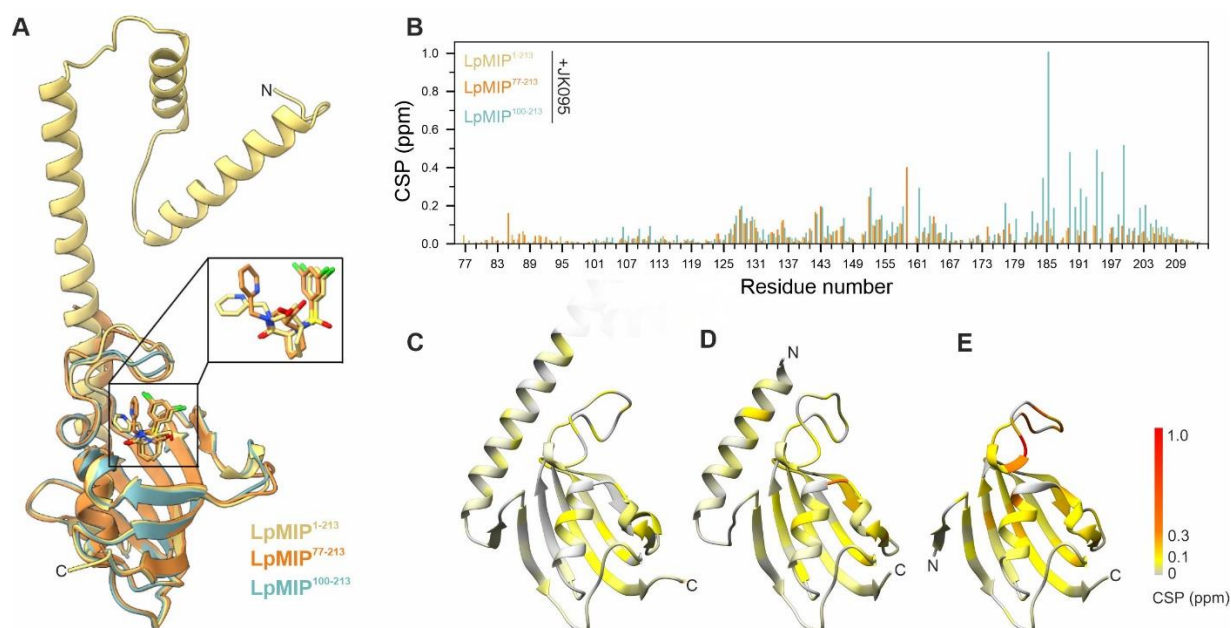
Fig. 5: Stalk helix affects interaction of *Lp*MIP FKBP-like domain with a [4.3.1]-aza-bicyclic sulfonamide inhibitor.

(**A**) Overlay of the X-ray crystal structures of *Lp*MIP[1-213] (full-length), *Lp*MIP[77-213] and *Lp*MIP[100-213] co-crystallized with JK095 (PDB IDs: 8BJD, 8BK5, 8BK6). For the *Lp*MIP[1-213] homodimer, only one subunit is shown. *Lp*MIP[100-231] also crystallizes as a dimer, but no clear density for the ligand was obtained (for details see main text and compare Fig. S8). In the zoom-in, not that in *Lp*MIP[77-213], the hydroxymethyl group of JK095 was found to adopt two different conformations.

(**B**) Chemical shift perturbations in the FKBP-like domain of ^{15}N-labeled full-length *Lp*MIP (yellow), *Lp*MIP[77-213] (orange) and *Lp*MIP[100-213] (teal) upon titration with JK095. For better comparison between the three constructs, a unified scale normalized to the maximal shift value in the FKBP-like domain across all three data sets was used.

(**C-E**) JK095-induced chemical shift perturbations within the FKBP-like domain plotted on crystal structures of full-length *Lp*MIP (C), *Lp*MIP[77-213] (D) and *Lp*MIP[100-213] (E).
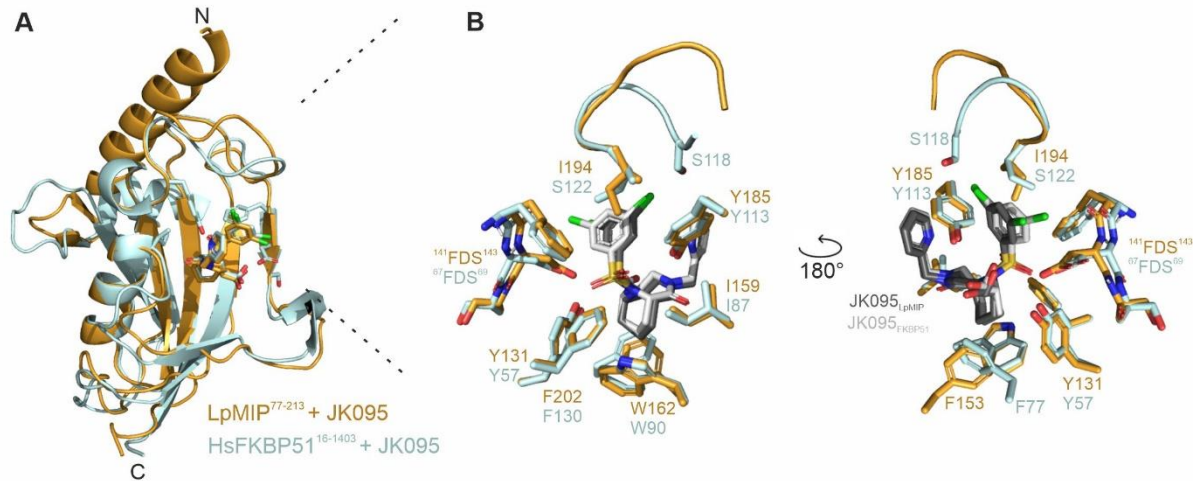
Fig. 6: Comparison of *Lp*MIP and human FKBP51 in complex with the bicyclic inhibitor JK095.

(**A**) Overlay of the crystal structures of *Lp*MIP$^{77\text{-}213}$ (PDB: 8BK5, orange) and FKBP51$^{16\text{-}140}$ (PDB: 50BK, cyan) in complex with the [4.3.1]-aza-bicyclic sulfonamide JK095.

(**B**) Zoom into the binding site. The relevant interacting residues are shown as sticks. JK095 is shown in dark (*Lp*MIP$^{77\text{-}213}$) or light (FKBP51$^{16\text{-}140}$) grey.
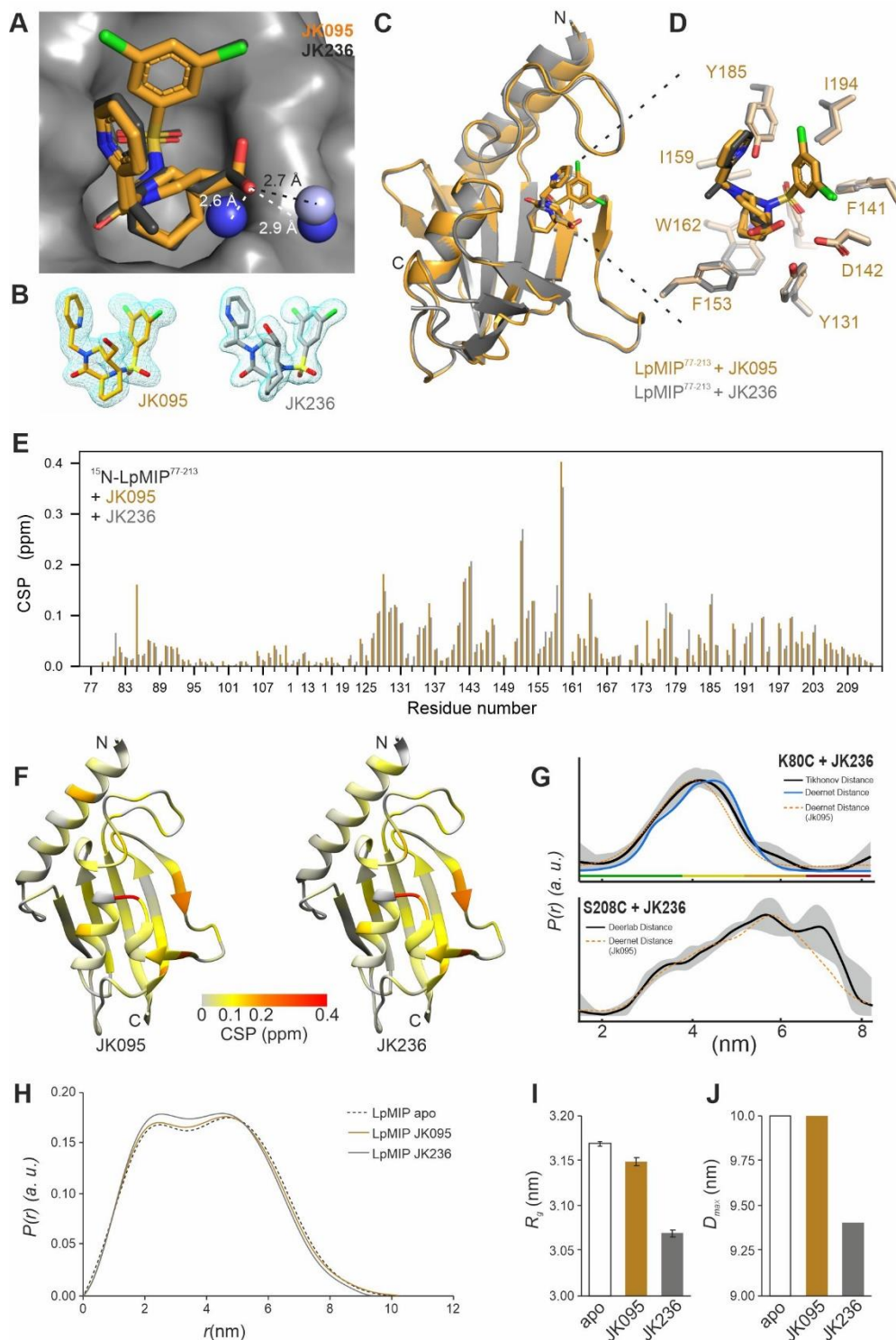
Fig. 7: Solvent exposed methyl group in [4.3.1]-aza-bicyclic sulfonamide inhibitor improves affinity for
*Lp*MIP[77-213] **through surface water displacement.**

(**A**) Water molecules in the crystal structures of *Lp*MIP[77-213] with JK095 (PDB: 8BK5, dark blue spheres) and
JK236 (PDB: 8BJE, light blue sphere). The additional methyl group in JK236 (pointing out of the paper plane)
displaces one of the two water molecules that forms a hydrogen bond with the inhibitor's hydroxymethyl group.

Distances between crystallographic water and the inhibitors are indicated by white (JK095) and black (JK236) dashed lines.

(**B**) Electron densities for the two inhibitor molecules in the co-crystal structures with LpMIP[77-213]. Note that for JK095, the hydroxymethyl group adopts two conformations.

(**C**) Overlay of the crystal structures of LpMIP[77-213] in complex with JK095 (PDB: 8BK5, orange) and its methylated derivative, JK236 (PDB: 8BJE, grey). For a structural comparison of the two molecules, see Scheme 1.

(**D**) Zoom into the binding site. The relevant interacting residues are shown as sticks.

(**E**) Relative NMR chemical shift perturbations (CSP) for JK095 (orange) and JK236 (grey) in comparison to the *apo* protein.

(**F**) Chemical shift perturbation shown in (E) mapped on the X-ray structure of LpMIP[77-213] (PDB: 8BK5).

(**G**) Measured spin label distances using PELDOR/DEER spectroscopy for spin-labeled full-length LpMIP K80C (top) or S208C (bottom) with JK236. For better comparison, the distance distribution for JK095 (see Fig. 3) is indicated as a dashed orange line (without error margins).

(**H**) SAXS derived real-space pair-distance distribution functions, or $p(r)$ profiles, calculated for LpMIP in the absence (dashed line) or presence of JK095 (orange line) or JK236 (grey line) and

(**I, J**) resulting R_g and D_{max} values. $p(r)$ functions were scaled to an area under the curve value of 1.
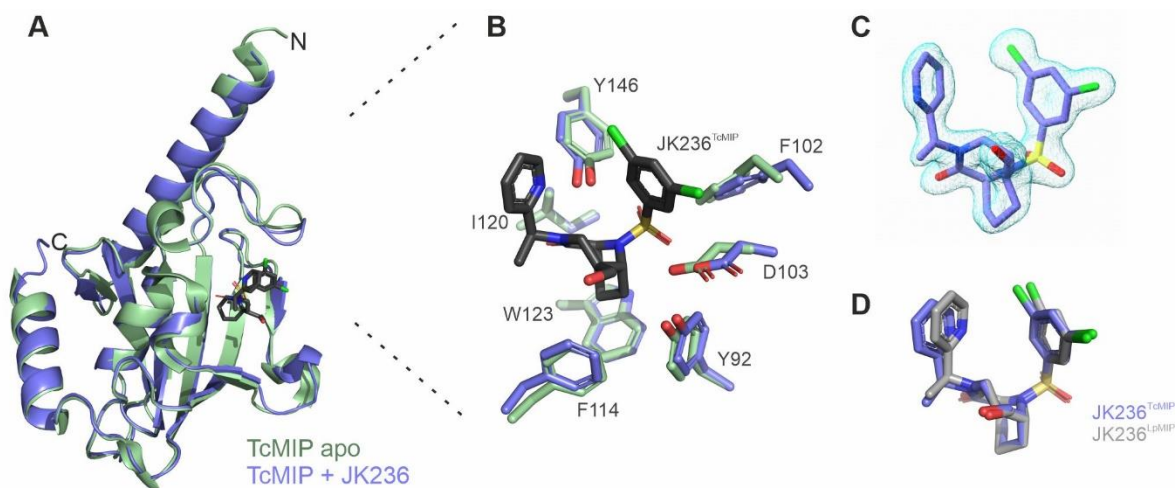
Fig. 8: *Trypanosoma cruzi* MIP in complex with a [4.3.1]-aza-bicyclic sulfonamide inhibitor.

(**A**) Overlay of the crystal structures of *apo Tc*MIP (green, PDB: 1JVW) and JK236-bound *Tc*MIP (blue, PDB: 8BK4).

(**B**) Active site residues in the *apo* or JK236-bound *Tc*MIP. The ligand is shown in black.

(**C**) Electron density for JK236 bound to *Tc*MIP. The 2Fo-Fc electron density maps are shown in light blue mesh at 3σ.

(**D**) Comparison of the inhibitor binding stance in *Tc*MIP (blue) and *Lp*MIP[77-213] (grey). For details, see also Fig. S9.